PHILOSOPHICAL TRANSACTIONS OF THE ROYAL SOCIETY A
MATHEMATICAL, PHYSICAL & ENGINEERING SCIENCES

The Response of the Thermosphere and Ionosphere to Magnetospheric Forcing

D. Rees and T. J. Fuller-Rowell

Phil. Trans. R. Soc. Lond. A 1989 **328**, 139-171
doi: 10.1098/rsta.1989.0029

Phil. Trans. R. Soc. Lond. A **328**, 139–171 (1989)
Printed in Great Britain

The response of the thermosphere and ionosphere to magnetospheric forcing

By D. Rees and T. J. Fuller-Rowell

Department of Physics and Astronomy, University College London, Gower Street, London WC1E 6BT, U.K.

[Plates 1–4]

During the past six years, rapid advances in three observational techniques (ground-based radars, optical interferometers and satellite-borne instruments) have provided a means of observing a wide range of spectacular interactions between the coupled magnetosphere, ionosphere and thermosphere system. Perhaps the most fundamental gain has come from the combined data-sets from the NASA *Dynamics Explorer* (*DE*) Satellites. These have unambiguously described the global nature of thermospheric flows, and their response to magnetospheric forcing. The *DE* spacecraft have also described, at the same time, the magnetospheric particle precipitation and convective electric fields which force the polar thermosphere and ionosphere. The response of the thermosphere to magnetospheric forcing is far more complex than merely the rare excitation of 1 km s^{-1} wind speeds and strong heating; the heating causes large-scale convection and advection within the thermosphere. These large winds grossly change the compositional structure of the upper thermosphere at high and middle latitudes during major geomagnetic disturbances. Some of the major seasonal and geomagnetic storm-related anomalies of the ionosphere are directly attributable to the gross wind-induced changes of thermospheric composition; the mid-latitude ionospheric storm 'negative phase', however, is yet to be fully understood. The combination of very strong polar wind velocities and rapid plasma convection forced by magnetospheric electric fields strongly and rapidly modify F-region plasma distributions generated by the combination of local solar and auroral ionization sources. Until recently, however, it has been difficult to interpret the observed complex spatial and time-dependent structures and motions of the thermosphere and ionosphere because of their strong and nonlinear coupling. It has recently been possible to complete a numerical and computational merging of the University College London (UCL) global thermospheric model and the Sheffield University ionospheric model. This has produced a self-consistent coupled thermospheric–ionospheric model, which has become a valuable diagnostic tool for examining thermospheric–ionospheric interactions in the polar regions. In particular, it is possible to examine the effects of induced winds, ion transport, and the seasonal and diurnal U.T. variations of solar heating and photoionization within the polar regions. Polar and high-latitude plasma density structure at F-region altitudes can be seen to be strongly controlled by U.T., and by season, even for constant solar and geomagnetic activity. In the winter, the F-region polar plasma density is generally dominated by the effects of transport of plasma from the dayside (sunlit cusp). In the summer polar region, however, an increase in the proportion of molecular to atomic species, created by the global seasonal circulation and augmented by the geomagnetic forcing, controls the plasma composition and generally depresses plasma densities at all U.Ts. A number of these complex effects can be seen in data obtained from ground-based radars, Fabry–Perot interferometers and in the combined *DE* data-sets. Several of these observations will be used, in combination with simulations using the UCL–Sheffield coupled model, to illustrate the major features of large-scale thermosphere–ionosphere interactions in response to geomagnetic forcing.

1. Background and introduction

1.1. *Review*

The major purpose of this review is to present a summary of recent advances in both experimental observation and numerical simulation of the terrestrial thermosphere. In the context of the discussion meeting, the presentation will concentrate on the behaviour of the high-latitude regions, where the influences of the magnetosphere are most strongly imprinted. These results will be interpreted, at least in part, by using global coupled numerical models of the thermosphere and ionosphere. The present status of coupled models will also be discussed, identifying the major outstanding problems of concept, theory and empirical data.

At all times and at all geomagnetic activity levels, the magnetosphere imprints unmistakable signatures upon the high-latitude thermosphere and ionosphere. The regions of such imprints recede poleward, away from areas of significant population, and thus historical observations, when the magnetosphere is in a 'quiescent' state. However, recent global observations from satellites, and new ground-based polar cap observatories have shown clearly that ionospheric structures, and thermospheric winds, temperature and composition are persistently disturbed in the vicinity of the auroral oval and within the geomagnetic polar cap. These disturbances are always collocated with signatures of energetic particle precipitation and convective electric fields, or else represent 'fossils' of strong forcing during the previous 24 h period.

A survey of the nature of the magnetospheric input and consequent thermospheric and ionospheric response, from quiet to very disturbed conditions, will thus be presented. The auroral oval generally expands equatorward and broadens as the level of geomagnetic activity increases. This expansion, broadening and an intensification of auroral precipitation is well shown in statistical surveys and analyses of the energetic electron precipitation (Hardy *et al.* 1985; Fuller-Rowell & Evans 1987), and is illustrated in figure 1, plate 1. These statistical surveys complement the impression obtained from individual observations. Analyses of polar plasma convection (Heppner 1977; Heppner & Maynard 1987; Foster *et al.* 1986) also show that the regions of strong magnetospheric convection electric fields imprinted on the polar ionosphere undergo a similar and closely related equatorward expansion and intensification (also in figure 1) as magnetospheric activity increases. Convection electric fields drive ionospheric plasma to velocities of the order of 1 km s^{-1}. The ions impart momentum to the neutral gas by means of 'ion drag', at the same time losing a little of their net ($\boldsymbol{E} \times \boldsymbol{B}$) velocity, creating the dissipative Pedersen ionospheric current component which causes Joule heating. If there is to be any effective energy or momentum transfer from the solar wind, via the magnetopause and magnetosphere to the ionosphere and thermosphere, alternating and direct current (AC and DC) components of the field-aligned current (Birkeland current) are required. Such magnetospheric currents are associated with the dissipative Pedersen current within the auroral ionosphere (component parallel to the ionospheric electric field). Both the field-aligned currents and the Pedersen currents within the auroral ionosphere intensify sharply as geomagnetic activity increases. The efficiency of momentum transfer and the Joule heating both increase linearly with ionospheric plasma density. Since Joule heating almost always considerably exceeds direct particle precipitation, knowledge of the ionospheric plasma response to precipitation is particularly important. The polar regions which display the imprints of these important phenomena of magnetospheric origin also show a wide range of other disturbances. These disturbances produce a range of characteristic signatures in the charged and energetic particle populations, the AC and DC electric and magnetic fields, and the optical aurora. However, for the moment we will concentrate on those phenomena which have the most direct connection to excitation of the thermosphere.

The signature of increasing geomagnetic activity, i.e. of intensifying convective electric fields and precipitation, and an equatorward expansion of the regions affected, implies also that field-aligned currents, Joule heating and ion-drag wind acceleration all increase. The temporal and spatial variability of all of the previously mentioned terms – 'geomagnetic forcing' – also increases, particularly at very high activity levels. Disturbances of the lower regions of the ionosphere, up to the normal E-region peak near 105–120 km, respond directly to 'auroral' inputs. At higher levels, strong interactions between the ionosphere and the induced chemical and dynamical changes of the thermosphere cause the ionospheric response to become much more complex, and rather more difficult to model and interpret. Global-scale disturbances within the thermosphere follow the initial high-latitude forcing. Propagating waves, and the consequences of gross wind-driven compositional changes have truly global consequences for the thermosphere, and force some very large, and long-lasting, disturbances of the ionosphere. During major geomagnetic disturbances, decay of ring-current energetic particles, probably mainly ions (Tinsley *et al.* 1988) appears to directly cause low-latitude disturbances of the thermosphere and ionosphere which are, as yet, rather difficult to include in a coherent and self-consistent model of the entire coupled solar–terrestrial system.

1.2. *Observational methods*

The observational results which will be discussed are based on three experimental systems which have been successfully adapted to observing the high-latitude thermosphere during the past decade. The bulk of the data come from the *Dynamics Explorer* satellites, and from ground-based Fabry–Perot interferometers, augmented by additional ground-based data from the incoherent-scatter radars at the European facility (EISCAT), Millstone Hill and Sondre-Stromfjord.

Dynamics Explorer 2 (*DE*2) carried two wind-measuring instruments, the Fabry–Perot interferometer (FPI, Hays *et al.* 1981) and the wind and temperature sensor (WATS, Spencer *et al.* 1981). The FPI observed meridional winds, and the WATS the zonal component. These could be combined, as demonstrated by Killeen *et al.* (1983) to give the full wind vector at upper thermospheric altitudes. *DE*2 also carried an effective battery of instruments capable of observing a wide range of ionospheric properties (Hoffman & Schmerling 1981) and the major elements of the magnetospheric input to the high-latitude ionosphere and thermosphere. *DE*1, from a more elliptical orbit, was additionally able to map large-scale auroral images, and further study the detailed physics of magnetospheric processes and interactions out to about $4R_E$ ($R_E = 6.37 \times 10^6$ m). The scope of the *DE*2 instrumentation for recording and interpreting polar thermospheric wind systems can be gleaned from the series of papers by using and interpreting the new results, for example Hays *et al.* (1984), Killeen *et al.* (1983, 1985, 1986), Rees *et al.* (1983, 1984, 1986) and Roble *et al.* (1983, 1984).

FPIs had been used quite early from the ground to study various airglow emissions, and were adapted to observe auroral emissions, line widths and Doppler shifts as early as the 1960s (see, for example, Armstrong 1969). However, it was the period of the late 1970s and early 1980s which saw the effective and systematic application of the high-resolution FPI to study the behaviour of high-latitude thermospheric winds.

The series of technical improvements in instrument resolution, stability and sensitivity, and matching improvements in the cost-effectiveness of semiautomated or fully automated operating and data acquisition systems can be best understood by following papers by Hays *et al.* (1979), Smith & Sweeney (1978), Rees *et al.* (1980, 1981, 1982), Meriwether *et al.* (1984). Meriwether (1983) provides a review of many of the major advances, and Hernandez (1986) and Hernandez & Killeen (1987) further review instrumentation methods, and recent scientific advances using FPIs for thermospheric research.

It was recognized quite early that one of the valuable physical quantities, which could be directly obtained from incoherent scatter radar (ISR) Doppler shift data, was ion drift velocity. Given ion drift vectors and plasma density as a function of altitude, the neutral wind speed may be deduced. In the F-region, the ion drift component along the local magnetic field is due to a combination of a parallel electric field component, gravity, the component of the meridional neutral wind resolved along the magnetic field and ambi-bipolar diffusion (Banks & Kockarts 1973; Rishbeth 1972). This method has been demonstrated to produce reliable meridional neutral wind values, in accurate agreement with ground-based optical interferometric observations (Rees *et al.* 1984; Wickwar *et al.* 1987; Meriwether *et al.* 1985; Winser *et al.* 1989), with the obvious advantage that observations can be continued through cloudy periods and during sunlit periods.

One of the major components in the ion thermal equation (Banks & Kockarts 1973) is the ion–neutral frictional heating term due to the differential velocity of ions and neutrals. The ISR measures perpendicular ion drifts and ion temperature, and the meridional neutral wind can be deduced from the parallel component of ion drift. In principle, therefore, the zonal neutral wind is the only unknown in the ion thermal equation. Unfortunately, the local neutral temperature is an essential baseline for the calculation, and the most appropriate value cannot be easily or accurately derived from atmospheric models. An appropriate value may be derived from other local measurements, such as those from an FPI (Rees *et al.* 1984). Thus far, a satisfactory analysis method of deducing zonal neutral flows in the upper thermosphere at high latitudes from ISR data alone has not been well demonstrated by intercomparison, although some very interesting experiments have been presented by Alcayde & Fontanari (1986) and Alcayde *et al.* (1986).

Even with the experimental technique advances described earlier, the database which is available is fragmentary: individual instruments, individual stations, individual satellite orbits; many of the most interesting results are the result of serendipity. Recently, wide-scale, coordinated observing campaigns, starting in the era of the *DE*2 satellite, and continuing as coordinated optical and radar observing programmes such as GISMOS, GITCAD, WAGS,† etc. have started to provide data on a truly global basis. Future programmes such as the Lower Thermosphere Coupling Study (LTCS) will contribute further as the number and capability of individual stations increases under the sponsorship of major initiatives such as the National Science Foundation Coupled Energetics and Dynamics of the Atmospheric Region (CEDAR).

1.3. *Numerical models*

To understand the thermosphere, it is necessary to cope with the fragmentary nature of available empirical data. The magnetospheric driving forces are complex, and the response of

---

† Global Ionospheric Simultaneous Measurements of Substorms, Global Ionospheric–Thermospheric Coupled Atmospheric Dynamics, World Atmospheric and Gravity Wave Study.

the stratified, always changing, thermospheric fluid is complex and nonlinear. There are also a number of poorly understood feedback mechanisms involving the plasma of the ionosphere, embedded within and originating from the thermospheric fluid. Numerical models provide little direct assistance with physics or empirical inputs which are not well determined, but do provide a global framework incorporating the basic, well-understood mechanisms and phenomena. Such models need to be global, and also time-dependent to be useful, as that is the nature of the thermosphere. Because we are not sure that our understanding of the nature of all the thermospheric driving forces is complete, and our empirical description of the temporal and spatial dependence of even the major solar and magnetospheric driving forces is still quite inadequate, numerical models have to be used wisely. They provide a good means of predicting the qualitative nature of the mean structure and of seasonal and solar activity variations. The general form of major large-scale thermospheric disturbances, the signatures of major magnetospheric disturbances, can be simulated quite well.

However, numerical models have to be used carefully in the prediction of thermospheric meteorology, particularly when small-scale and short-period disturbances are of interest. This is not particularly because of any problems of the models themselves, but simply reflects our lack of meteorological information on the variations of the magnetosphere and the ionosphere, through which most magnetosphere inputs are imparted, directly or otherwise, to the thermosphere.

Numerical simulation of the thermosphere from first principles requires that the most important physical processes occurring within the thermosphere are properly treated (Fuller-Rowell & Rees 1980, 1983; Dickinson *et al.* 1981, 1984; Roble *et al.* 1982). It can be assumed that most of the energy and momentum sources driving the thermosphere are predetermined, and invariant to the response of the thermosphere. The thermosphere does not determine the nature of the solar ultraviolet and extreme ultraviolet (UV and EUV) inputs which provide important heat and ionization sources. However, the thermosphere does react strongly to forcing. The major responses in wind, temperature and composition of the polar thermosphere to ion convection and heating within the auroral oval and polar cap are now well documented by ground-based and spaceborne observation (Hays *et al.* 1984; Rees *et al.* 1983, 1985, 1986). Some of these thermospheric responses may change the nature or magnitude of the forcing itself. While this review will concentrate on external thermospheric forcing from the magnetosphere, it should be noted that significant effects, particularly in the lower thermosphere, occur from internal forcing from the lower atmosphere, as a result of the combination of tidal waves, gravity waves and planetary waves. The first can be handled numerically within a thermospheric model by introducing a 'flexible' lower boundary, where self-consistent changes of wind and temperature correspond to the amplitudes and phases of specific propagating tidal modes. The actual propagation of such tides through the lower and middle atmosphere is not simulated by such a procedure, however, the amplitudes and phases of several modes can be adjusted, by experiment, until the results within the lower thermosphere correspond to observed variations of tidal phases in temperature and wind (etc.) as functions of altitude, season and latitude. It is found, as would be expected, that the relatively large amplitudes of observed tidal winds in the lower thermosphere can be successfully simulated by introducing such propagating tides. This is not possible, if only the *in situ* generated tides are considered. Additionally, large nonlinear interactions occur between the individual propagating tidal modes themselves, and between them and the *in situ* tides.

While these studies still have to be considered as experimental (because the real tidal and meteorological behaviour of the middle atmosphere is still virtually unknown), these studies (Fesen *et al.* 1986) do provide a very useful insight into the complexities of the thermosphere.

The most fundamental influence of the magnetosphere on the thermosphere comes from magnetospheric plasma convection. This convection drives rapid motion of plasma throughout the polar cap and auroral oval. The structure and variability of polar convective fields were not well understood until the late 1960s and early 1970s, with the advent of rocket and satellite measurements of ion drifts and electric fields (Heppner 1977; Heppner & Maynard 1987). These rapid plasma motions accelerate the auroral thermosphere by means of the process commonly known as ion drag (Rishbeth 1972).

The resulting ion–neutral frictional drag causes direct heating of both ions and neutrals, commonly known as Joule heating (Cole 1962, 1971). Induced winds may increase or decrease (but generally decrease) the ion drag, and the resulting frictional heating. The induced winds (or more correctly, changed winds, since there is always a complex wind system in existence before a given geomagnetic disturbance) may induce a 'back-electromotive-force' ('back-EMF'), opposing the initial magnetospheric convective electric field. This wind system (subtly modified by gas pressure changes due to neutral heating) will also induce ion drifts (or change in ion drifts) parallel to the local magnetic field. Such 'parallel' ion drifts will also induce a field-aligned electron flow, to maintain quasi-charge neutrality. Thus the entire vertical plasma distribution will respond to wind changes, an effect which becomes increasingly important at greater altitudes. This change of ion density distribution will modify the consequent ion drag on the neutrals, and thus the wind acceleration terms, and finally the winds themselves. Because, in the vicinity of the auroral oval and polar cap, there are always various contra-flowing streams of field-aligned thermal and suprathermal particles, it is difficult to identify the net field-aligned current by direct observation. Yet it is the net flow which powers the magnetosphere–thermosphere forcing process, and variations of this field-aligned flow caused by feedback processes are important, but necessarily second-order changes, and thus difficult to observe directly.

Large changes of upper thermospheric composition are induced by combined advection and convection, resulting from strong thermospheric heating in the polar regions. These composition changes (and specifically, enhanced concentrations of molecular nitrogen) are particularly pronounced at F-region heights during geomagnetic storm periods and within the summer geomagnetic polar region. Enhanced concentrations of molecular nitrogen cause significant depletions of F-region plasma densities by greatly increasing the effective recombination coefficient, while the ionization rates, due to the combination of solar photoionization and auroral precipitation, are only slightly changed.

At E-region altitudes, induced wind changes, particularly those caused by ion drag, generally reduce the effective EMF, thus decreasing the effective ion drag acceleration (limiting the maximum induced winds). The induced winds also tend to decrease the local electrojet current (at all heights), as the electromotive force $e(\boldsymbol{E}+\boldsymbol{V}_n\times\boldsymbol{B})$ is decreased. These processes are independent of any plasma density and conductivity modifications, however, the thermosphere will respond to both processes (changed electromotive force and electrojet current and consequent heating).

Any modifications of the horizontal current (usually decreases) due to the induced winds, will change the capacity of the ionosphere to carry field-aligned currents (FAC) which connect to the magnetosphere. Intuitively, the feedback effects of the induced winds on the total electromotive force, and the modified capacity of the auroral ionosphere to transmit or connect the FAC might be expected to cause some significant effects on the magnetosphere at times of large disturbances (when the E-region winds are known to reach 50% of the $\boldsymbol{E}\times\boldsymbol{B}$ ion drift velocity, driven by magnetospheric electric fields; see, for example, Rees 1971, 1973; Pereira *et al.* 1980).

Although some numerical experiments in these areas are in progress (see, for example, Harel *et al.* 1981), theoretical and experimental exploration of these problems is still at a very preliminary phase. We do not understand whether limits of the availability of charge carriers (ionospheric or magnetospheric) are important. Slight changes of the FAC may be matched by compensating changes in field-aligned potentials. Alternatively, slight shifts may occur in the patterns of overall magnetospheric convection, or its mapping to the ionosphere, to compensate for thermospheric or ionospheric feedback processes (Fuller-Rowell *et al.* 1987*a*). Feedback processes within the thermosphere and ionosphere probably affect a number of magnetospheric processes which have, historically, been thought of as purely magnetospheric or plasma physics phenomena.

The processes by which interactions between the polar ionosphere, thermosphere and magnetosphere occur, and the major routes by which feedback can occur, are easy to describe intuitively. However, the thermosphere and ionosphere are so closely interwoven by chemistry, dynamics and energetics, that quantitative modelling cannot rely on an intuitive approach.

The earliest global three-dimensional time-dependent numerical thermospheric models (Fuller-Rowell & Rees 1980, 1983; Dickinson *et al.* 1981, 1984; Roble *et al.* 1982) used theoretical or simple empirical models of the ionosphere, based on the Chiu (1975) global model to calculate ion drag and Joule heating. However, the lack of any response of the Chiu ionospheric model at high latitudes to geomagnetic processes (precipitation, convection) caused a gross underestimate of the magnitude of ion drag and of Joule or frictional heating at E-region altitudes in the auroral oval. The F-region plasma densities were not so seriously underestimated, and the Chiu model, used in conjunction with the three dimensional, time-dependent models (or general circulation models, GCMS) simulated more realistic F-region winds and temperatures of the thermosphere (Rees *et al.* 1985, 1986).

However, the underestimate of E-region forcing and heating caused very serious problems in simulations of the geomagnetic response in neutral chemistry and in total density, as well as the E-region winds, etc. (Rees *et al.* 1985, 1986). Thus a series of numerical experiments were started to find methods of coping more realistically with the underlying difficulty, which is how to simulate the mutual interactions of the polar ionosphere and thermosphere.

The first serious efforts to create an interactive model for the polar ionosphere and thermosphere were published by Quegan *et al.* (1982) and Fuller-Rowell *et al.* (1984). In this model, data-sets from a global thermosphere (University College London (UCL)) and the 'Sheffield' polar ionosphere model (U.T.-independent) were iteratively exchanged until stability was achieved. The effects of the model iterations showed that significant changes in plasma density were caused by the effects of induced winds. The auroral oval plasma densities were greatly enhanced compared with those of the Chiu model. As a result, induced thermospheric winds and heating were generally greatly increased compared with previous simulations using the global Chiu (1975) model.

This 'simple' coupled model could not, however, be universally applied to study U.T.

variations, let alone the effects of variable solar, geomagnetic and seasonal conditions. The next stage, developing a fully interactive thermosphere and polar ionosphere model, was complex, and is described in some detail in a series of papers by Fuller-Rowell *et al.* (1987*b*, 1988) and by Rees & Fuller-Rowell (1987*a*, *b*). This fully coupled model, exchanges ionospheric and thermospheric parameters throughout the region poleward of 55° geomagnetic latitude. At lower latitudes, the numerical model is presently still dependent on empirical ionospheric descriptions. When the physical processes of the major ionospheric–thermospheric interactions are included self-consistently within the coupled model, *ad hoc* additional 'geomagnetic' energy sources which were required previously to explain observations are unnecessary (Rees *et al.* 1988).

2. THE COUPLED GLOBAL THERMOSPHERE–POLAR-IONOSPHERE MODEL

The development of the UCL three-dimensional thermospheric model is well documented in previous publications (Fuller-Rowell & Rees 1980, 1983), as is the Sheffield ionospheric model (Quegan *et al.* 1982, 1986). Progress with this model coupling has been reported in a number of papers during the past three to four years by Quegan *et al.* (1982), Fuller-Rowell *et al.* (1984), Fuller-Rowell *et al.* (1987*b*, 1988) and by Rees & Fuller-Rowell (1987*a*, *b*).

The UCL three-dimensional thermospheric model (or thermospheric TGCM) simulates the time-dependent structure of the vector wind, temperature, density and composition of the neutral atmosphere, by numerically solving the nonlinear equations of momentum, energy and continuity (Fuller-Rowell & Rees 1980), and a time-dependent mean mass equation (Fuller-Rowell & Rees 1983). The global atmosphere is divided into a series of elements in geographic latitude, longitude and pressure. Each grid point rotates with the earth to define a non-inertial frame of reference in a spherical polar coordinate system. The latitude resolution is 2°, the longitude resolution is 18°, and each longitude slice sweeps through all local times, with a 1 min time step. In the vertical direction the atmosphere is divided into 15 levels in log (pressure), each layer is equivalent to one scale height thickness, from a lower boundary of 1 Pa at 80 km height.

The time-dependent variables of southward and eastward neutral wind, total energy density and mean molecular mass are evaluated at each grid point by an explicit time stepping numerical technique. After each iteration the vertical wind is derived, together with temperature, heights of pressure surfaces, density, and atomic oxygen and molecular nitrogen concentrations. The data can be interpolated to fixed heights for comparison with experimental data, or with empirical models. The momentum equation is nonlinear and the solutions fully describe the horizontal and vertical advection, i.e. the transport of momentum.

The neutral atmosphere numerical model uses an eulerian approach. However, the ionospheric code (Quegan *et al.* 1982, 1986; Fuller-Rowell *et al.* 1987*b*, 1988) has to be evaluated in a lagrangian system. The complex convection patterns imposed by a magnetospheric electric field on plasma movements within the polar regions are referenced to a fixed Sun–Earth frame, assuming pure $\boldsymbol{E} \times \boldsymbol{B}$ drifts. The electric field is derived by merging a model of magnetospheric convection (for example one of the models presented by Heppner & Maynard 1987) with the corotation potential (induced by the Earth's rotation). Parcels of plasma are traced along their convections paths, which are often complex. Recently the ionospheric lagrangian frame of reference has been modified to be more compatible with the neutral eulerian frame, eliminating the need for 'corotation potential' and excessive coordinate system transformations. In the ionospheric code, atomic (H^+ and O^+) and molecular ion concentrations are evaluated over the height range 100–1500 km, and used in the thermospheric code within 35° magnetic latitude of the north and south magnetic poles.

To avoid further repetition of the details of the numerical codes, the reader is referred to the series of papers previously cited for details of the UCL thermospheric model (Fuller-Rowell & Rees 1980, 1983), for information on the Sheffield ionospheric code (Quegan *et al.* 1982, 1986; Watkins 1978; Allen *et al.* 1986) and for information on the procedures used to couple the UCL thermospheric and Sheffield polar ionospheric models (Fuller-Rowell *et al.* 1987*b*, 1988).

One major new upgrade of the coupled model will be introduced in this paper. Previously, as with the thermospheric GCM (from the National Center for Atmospheric Research), the UCL model had used an asymmetric offset dipole for the geomagnetic field description. This yielded some quite satisfactory results in comparison with many of the available ground-based and satellite data-sets. However, the real geomagnetic-field's coordinate system is significantly elliptical in the Northern Hemisphere (Gustaffson 1970), when projected onto a geographical reference frame. Figure 2 illustrates the mapping of ion-drifts and auroral ionization rate, from the activity level 7 magnetospheric input in figure 1, onto the geographic frame at 18 U.T. The distortion of the mapping can be clearly seen, the differences between semimajor and semiminor axes amounting to about 4° in the Northern Hemisphere (international geomagnetic reference field for 1980 (IGRF-1980)). In addition, the field strength and field orientation are quite variable, causing major changes in the computed ion drift vector, ion drag and electric current terms. Although sounding simple, the introduction of this change has caused several numerical and computational problems. Within this review a simulation incorporating the improved mapping by the IGRF magnetic field will be shown, however, differences due to the change of magnitude and direction of the field are not included in this paper.

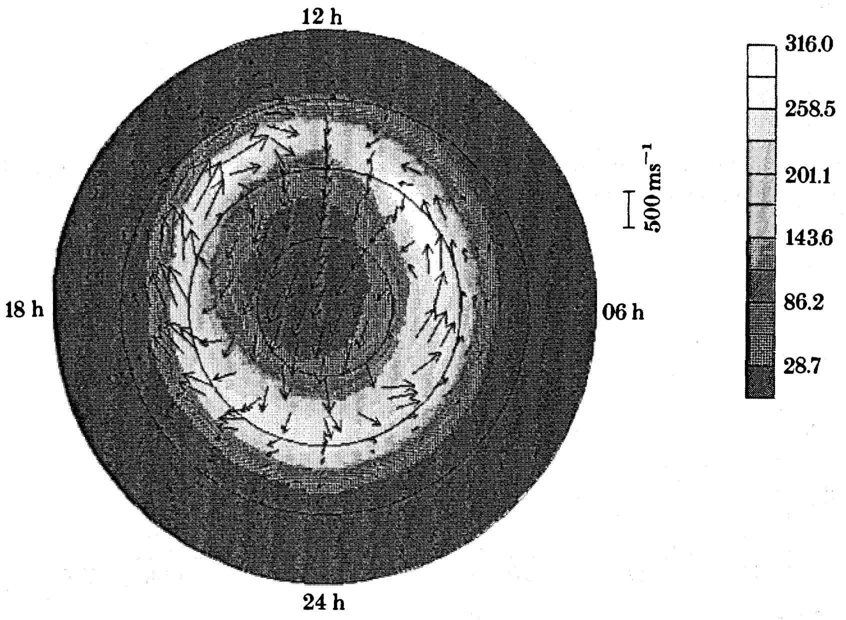

FIGURE 2. Ionization rate (in units of 10^6 m^{-3}) and ion drift vectors associated with activity level 7 of figure 1, as they are mapped onto the geographic high latitudes (50–90°) by the IGRF magnetic field. Data is from the UCL–Sheffield model for equinox conditions and low solar activity ($F_{10.7} = 80$, 23 September).

3. Observational results from the ground and from satellites

3.1. *Ground-based optical results*

Two particularly interesting sets of data from the UCL ground-based FPI located at Kiruna, northern Sweden (Rees *et al.* 1984, 1986) are presented in figures 3 and 4 respectively. The first data-set, figure 3, obtained during the night of 12/13 December 1981, shows the classical response of the thermosphere in the vicinity of the dusk auroral oval to a strong disturbance. The very strong westward (sunward) winds observed over a period of several hours corresponded to (mainly) ion drag forcing, at a time when the auroral oval was considerably expanded, with a cross-polar cap electric field reaching 150 kV, as measured by instrumentation on the *Dynamics Explorer* satellite. Auroral emissions throughout the entire auroral oval were strongly enhanced for a period of several hours (*ca.* 12–18h U.T.).

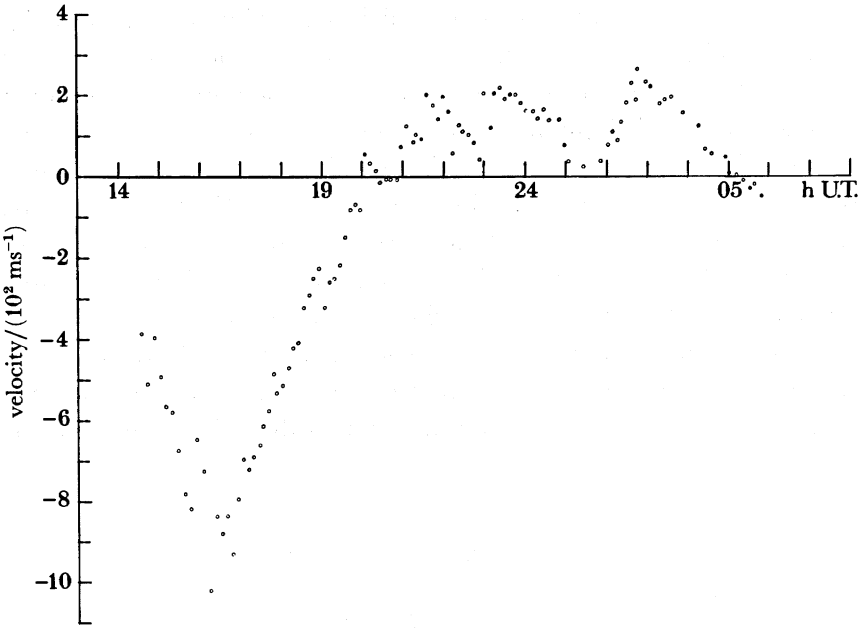

Figure 3. A period of intense westward winds in the dusk sector of the auroral oval, at a height of 240 km and as observed by a ground-based FPI on 12 December 1981, at Kiruna, Sweden. (Positive is eastward, negative is westward.)

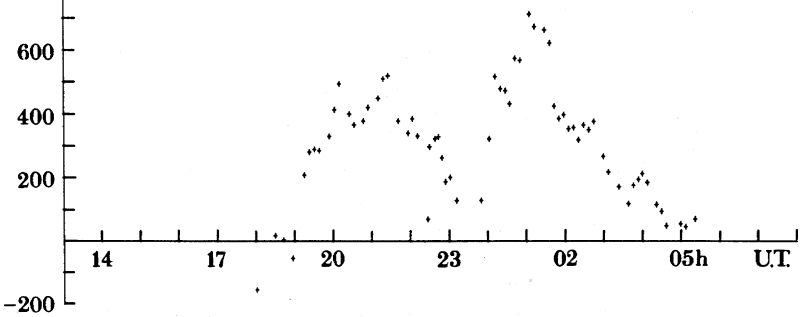

Figure 4. A period of intense eastward thermospheric winds in the dawn sector of the auroral oval, at a height of 240 km and as observed by a ground-based FPI on 12 February 1982, at Kiruna, Sweden.

Figure 4 shows a much more unusual situation, with 500–700 m s^{-1} sunward winds in the dawn auroral oval, which occurred during a time when a comparable equatorward component was present. These winds are rather more difficult to understand and simulate than those shown in figure 3. They were created during an extended, highly disturbed, period, when the IMF B_Y component was strongly negative, by the combination of strong eastward ion drag, and very strong antisunward winds blowing over the polar cap. Such large eastward winds in the dawn auroral oval are much rarer than the westward values of comparable magnitude in the dusk auroral oval shown in figure 3. The natural behaviour of the thermosphere tends to discriminate strongly against high-velocity cyclonic (anticlockwise) vortices in the vicinity of the dawn auroral oval or polar cap. On the contrary, as discussed by Fuller-Rowell & Rees (1984) and Fuller-Rowell *et al.* (1984), the anticyclonic (clockwise) vortex is relatively easily generated by a resonance between the rotating atmosphere and the anticyclonic plasma convection vortex within the dusk auroral oval and polar cap regions.

In figure 5*a–d* a statistical analysis of data obtained from the UCL ground-based FPI at Kiruna is shown. The wind velocity data are sampled by the daily sum of the local magnetic index *K*, and by U.T. (Rees *et al.* 1987). At low magnetic-activity levels, (figure 5*a*), the wind data are reminiscent of those expected for a low-latitude station, eastward winds in the evening, westward winds in the morning, equatorward winds near midnight. The only obvious influence of geomagnetic activity is that the equatorward winds near midnight are 150–200 m s^{-1}, rather than 100 m s^{-1}. At such low activity levels, the auroral oval is still a few hundred kilometres north (poleward) of Kiruna, even at magnetic midnight. At higher activity levels, (figure 5*b*), the evening behaviour of the winds changes sharply; the winds turn westward in the early evening hours, for a period of some hours. This is as a result of the direct influence of ion drag acceleration by ions convected sunward within the dusk auroral oval. Two model simulations are also shown in figure 5 (*e* and *f*) for very quiet and moderately disturbed geomagnetic conditions. The transition from eastward to westward winds in the evening sector is quite apparent as activity increases, and the agreement in magnitude and direction with the experimental data is quite encouraging. As the level of activity increases (figure 5*c*) the westward wind speed increases until, under very active conditions (figure 5*d*), the dusk auroral oval is found equatorward of Kiruna. Under such conditions, when Kiruna is on the polar cap boundary of the auroral oval, or even within the polar cap, the westward wind speed decreases.

Later in the U.T. day (or rather, night) there is a general increase of equatorward wind speed with increasing magnetic activity. The eastward (morning) wind component, on average, is much less than the westward evening component, as mentioned from the results of individual days and orbits. The other factor which is worth noting is that at all times, an increased activity level causes increased wind variability (speed and direction), as well as increased average velocities.

A general feature of Kiruna's location is that the auroral oval moves poleward in the early morning hours, and Kiruna is almost always equatorward of the oval by 06–08h U.T., even under extremely disturbed conditions.

3.2. *Ground-based radar results*

Although the major potential advantage of the ISR wind-measuring technique, compared with ground-based optical measurement of thermospheric winds, is the freedom from

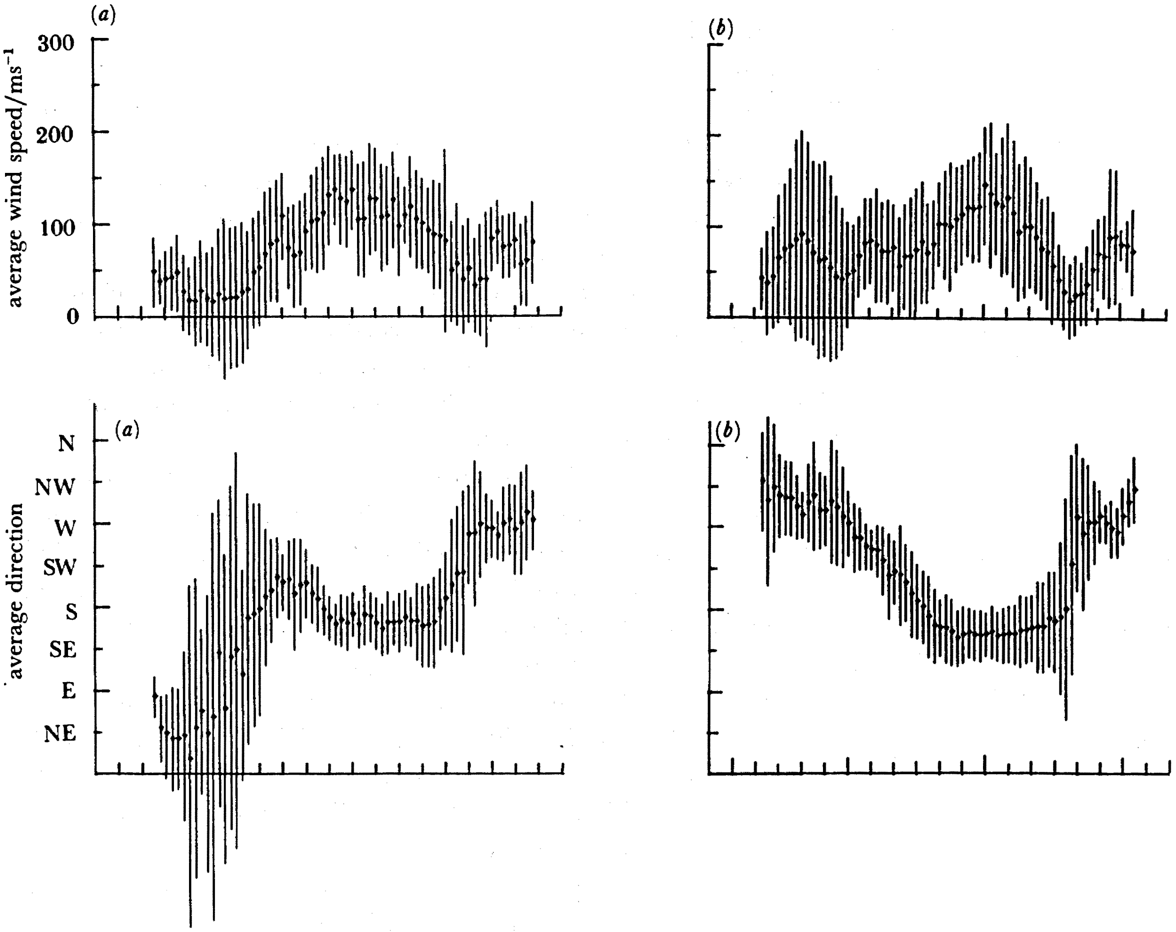

FIGURE 5. For legend see facing page.

interference by both cloud and daytime, so far, rather few data have been published. Alcayde & Fontanari (1986) discussed results from the EISCAT radar, presenting results which are generally consistent with numerical models and with optical interferometric results. In their figure 7 *a*, *b* a broad latitudinal band of sunward winds are observed in the dusk auroral oval, in keeping with the similarly directed but stronger sunward convective ion flows observed during those periods (6 March 1984, 28 June 1984). In the dawn auroral oval, the eastward neutral flows were deduced to be generally less organized and rather slower for the March day, but rather stronger and more uniform during the summer solstice observing period.

In other reported observations, it has been possible to make an intercomparison with ground-based optical wind measurements. The radar-derived meridional winds around 240–320 km are essentially identical to those obtained by optical interferometric methods (Wickwar *et al.* 1984), particularly when the effects of non-maxwellian ion velocity distribution (Rees *et al.* 1984), and the effect of the neutral vertical wind on the ion velocity component parallel to the magnetic field are allowed for (Winser *et al.* 1989). The zonal component is more difficult to deduce, with a number of contributing error terms, including those from the lack of independent knowledge of the baseline neutral temperature, the individual ion flow components, correction for vertical neutral wind (usually not known), and uncertainty in the

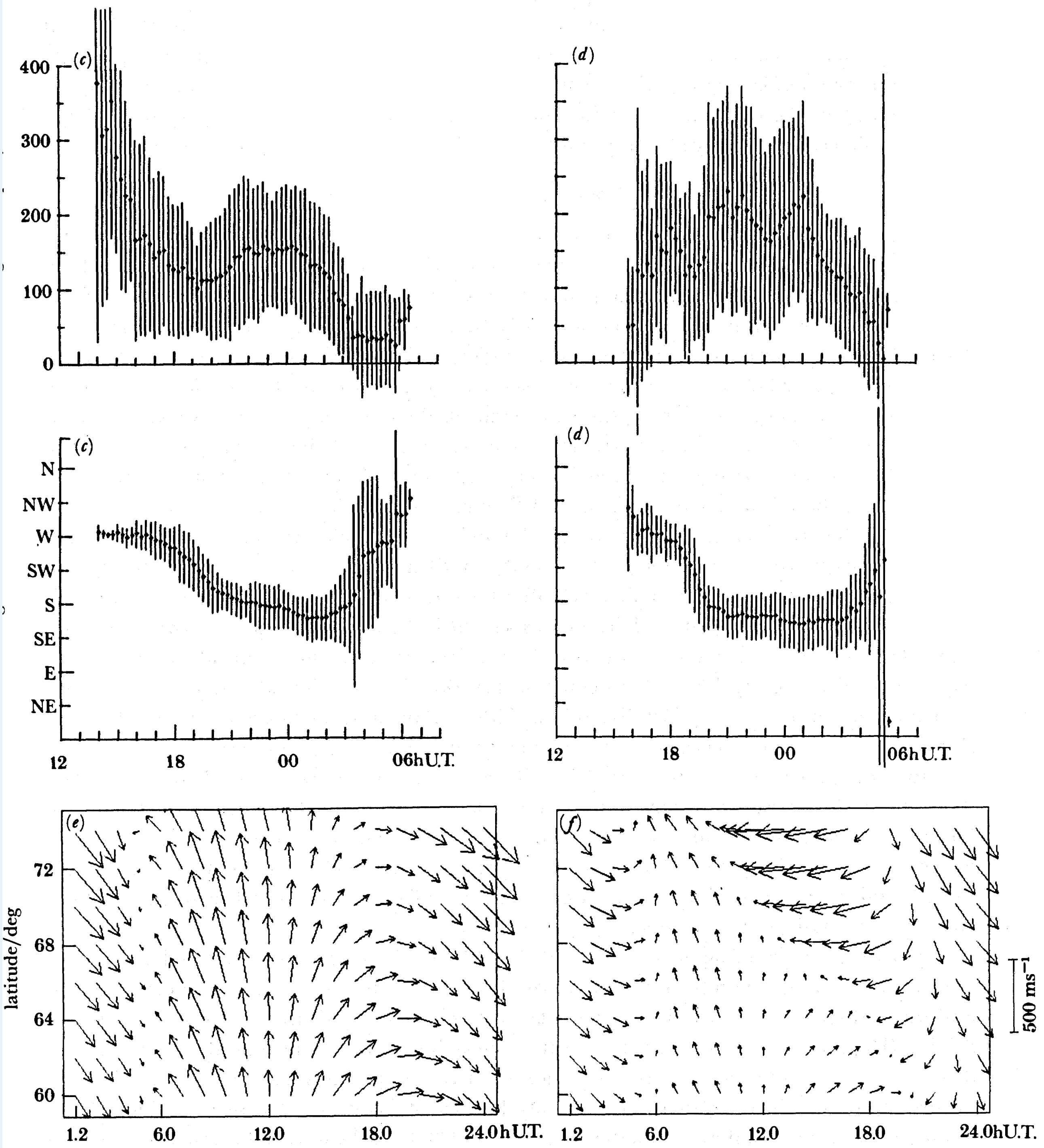

FIGURE 5. Statistical patterns of the magnitude and direction of the thermospheric neutral wind observed from Kiruna by the ground-based FPI at four magnetic activity levels, (*a*)–(*d*), together with model simulation predictions, (*e*) and (*f*). Kiruna wind flow ranges are (*a*) $0 < K\text{–sum} < 15$; (*b*) $15 < K\text{–sum} < 25$; (*c*) $35 < K\text{–sum} < 40$; (*d*) $40 < K\text{–sum} < 72$. The predictions are for (*e*) very quiet and (*f*) moderately disturbed conditions, high solar activity on 21 December at a longitude of 18° E.

O–O$^+$ collision frequency. The data published by Alcayde & Fontanari (1986) look quite convincing, but it is clear that the proper derivation required a considerable amount of careful analysis. It may be also that a fortunate combination of circumstances may permit a reliable derivation for one observing period, while similar quality raw data, at the time of a major disturbance, may prove difficult to interpret, because of, for example, strong neutral gas heating which cannot be keyed to a specific and available model of thermospheric temperature.

3.3. *Satellite-borne optical and in situ results*

The *Dynamics Explorer* satellites observed a wide range of geomagnetic activity conditions and individual events. Figure 6, plate 2, taken from Killeen *et al.* (1988), was obtained by combining wind data from the WATS and FPI instruments onboard *DE*2, with that of the spin–scan imager (Frank *et al.* 1981) onboard *DE*1. For each of the four intervals depicted, *DE*1 was near apogee over the northern polar region while *DE*2 was passing underneath, close to its perigee (near 300 km). All the results show the classical neutral wind signatures of the auroral oval and polar cap: strong sunward winds in the dusk auroral oval, weaker sunward winds in the dawn auroral oval (sometimes only a reduction of the antisunward flow). The polar cap contains a region of strong antisunward flow, while at lower latitudes than the auroral oval, there is a general antisunward flow of around 150–200 m s^{-1}.

The four events cover a very wide range of activity and detailed response. The extremes of activity are depicted by figure 6*b*, *d* (12 December 1981 and 15 December 1981, respectively). (*b*) shows the situation at 12h44 U.T., soon after the start of the very disturbed period for which the ground-based FPI data from Kiruna was shown in figure 3. The auroral oval is greatly expanded and very active, consistent with the peak winds of the dusk auroral oval and polar cap, which reach nearly 1 km s^{-1}. In contrast, (*d*) (05h05 U.T.) shows weak emissions and a contracted auroral oval, only just discernible. Although the auroral emission is weak, the wind signature is still distinct, even if the peak sunward values are less than 200 m s^{-1}.

Figure 6*a* (6 December 1981, 15h05 U.T.) shows a varied situation: there is a strong (600–800 m s^{-1}) antisunward flow in the polar cap, confined to the dawn side of the polar cap. On the dusk side, the antisunward flow is generally weak, and in fact there is a limited region of sunward flow. This period was one with a northward IMF field component, with relatively strong total magnetic field strength. Sunward winds in the dusk auroral oval are less than 300 m s^{-1}, a relatively weak value.

Figure 6*c* shows data from 6 December 1981, 08h38 U.T. (southward IMF). On this occasion, the sunward winds within the dusk auroral oval match the winds within the strong antisunward jet on the dawn side of the polar cap. The *Y*-component of the IMF was positive, driving (Heppner & Maynard 1987) a strong convection vortex connecting the dusk oval and dawn polar cap, and leaving weak convection (and very weak sunward winds, for a relatively disturbed period), in the dawn auroral oval. This can be contrasted with (*b*), which shows symmetric antisunward flow within the polar cap, and 300 m s^{-1} winds in the dawn auroral oval (30% of the peak dusk oval sunward winds). The *Y*-component of the IMF was rather small during most of the event of 12 December 1981.

Detailed analysis of the situations displayed in figure 6*a*, *c* are shown in figures 7 and 8, plates 3 and 4, respectively (also taken from Killeen *et al.* 1988). Included in these presentations are the additional data available from the ion drift meter (IDM, Heelis *et al.* 1981) and the Langmuir probe instrument (LAPI, Krehbiel *et al.* 1981). The former provides the electric field

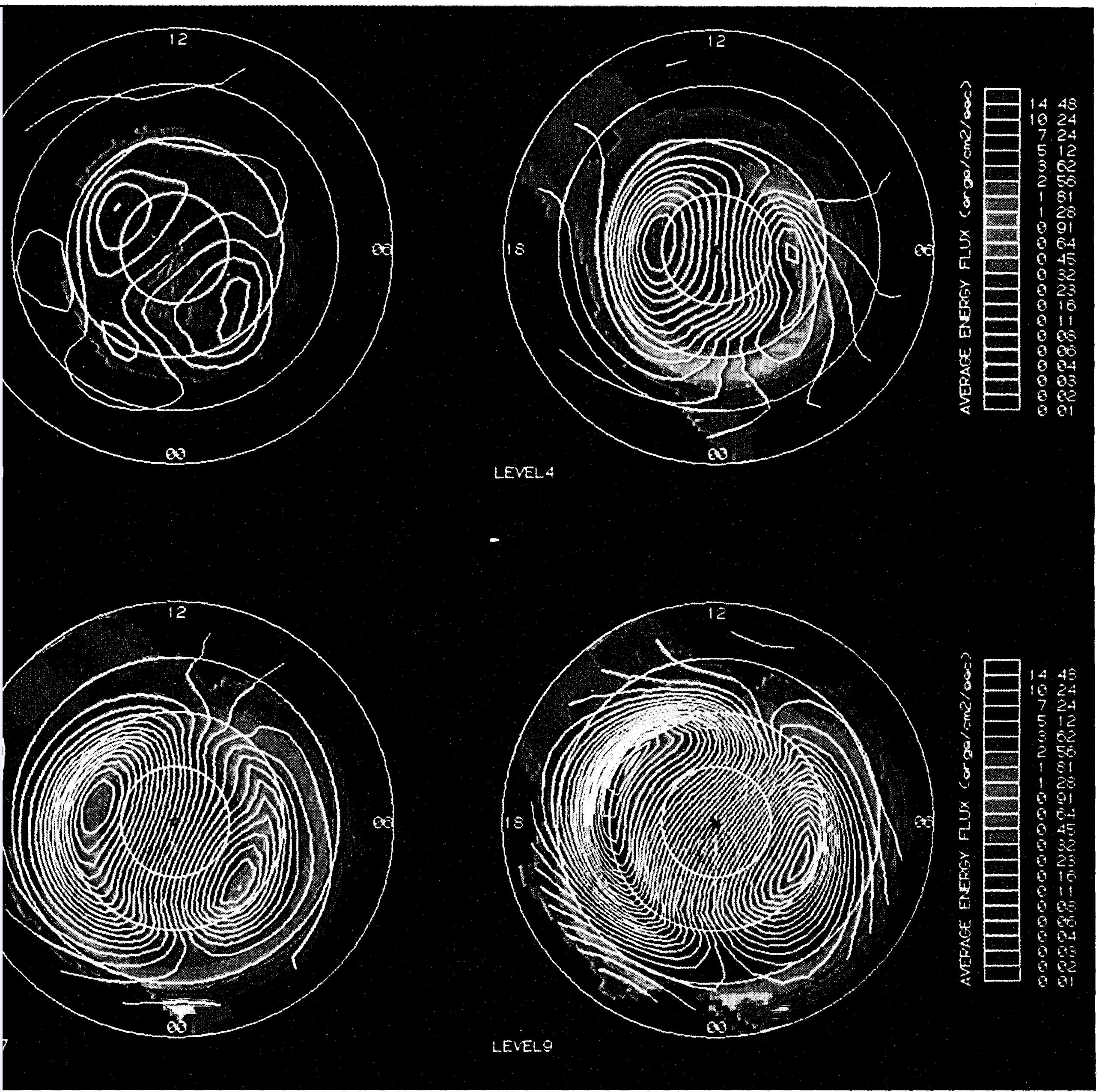

FIGURE 1. Statistical patterns of auroral particle energy influx (ergs per centimetre squared per second, 1 erg = 10^{-7} J) and equipotential convection contours for four increasing levels of geomagnetic activity.

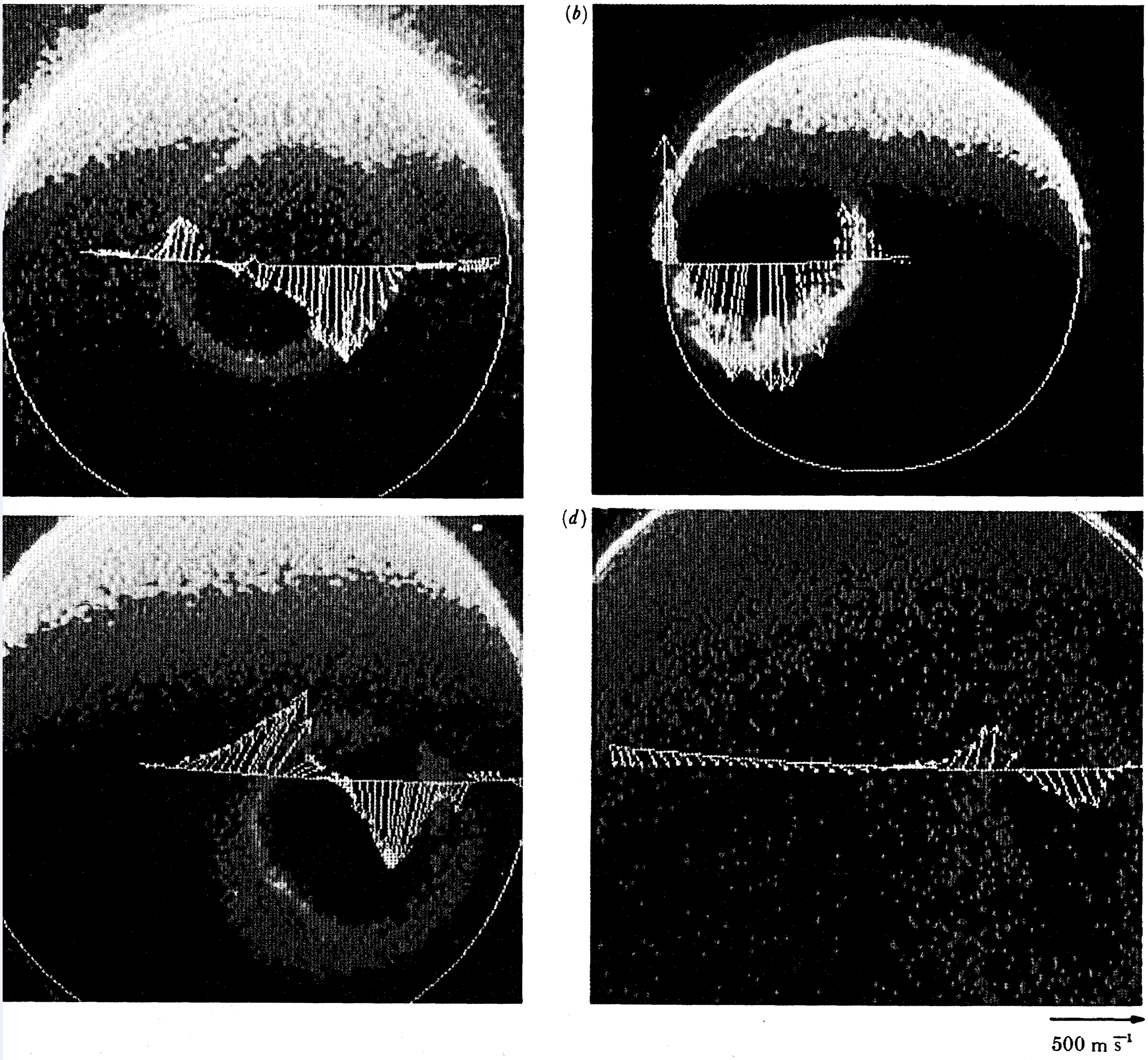

FIGURE 6. The *DE*2 and *DE*1 spacecraft simultaneously observed the northern auroral oval on a number of occasions during the winter of 1981–82 (Killeen *et al.* 1988). The observations were made on (*a*) 6 December 1981 at 15h05 U.T., orbit 1853; (*b*) 12 December 1981 at 12h44 U.T., orbit 1941; (*c*) 6 December 1981 at 08h38 U.T., orbit 1849; (*d*) 15 December 1981 at 05h05 U.T., orbit 1981. *DE*2 provided the wind vectors, while the large-scale auroral images were obtained from the *DE*1 spin-scan imager.

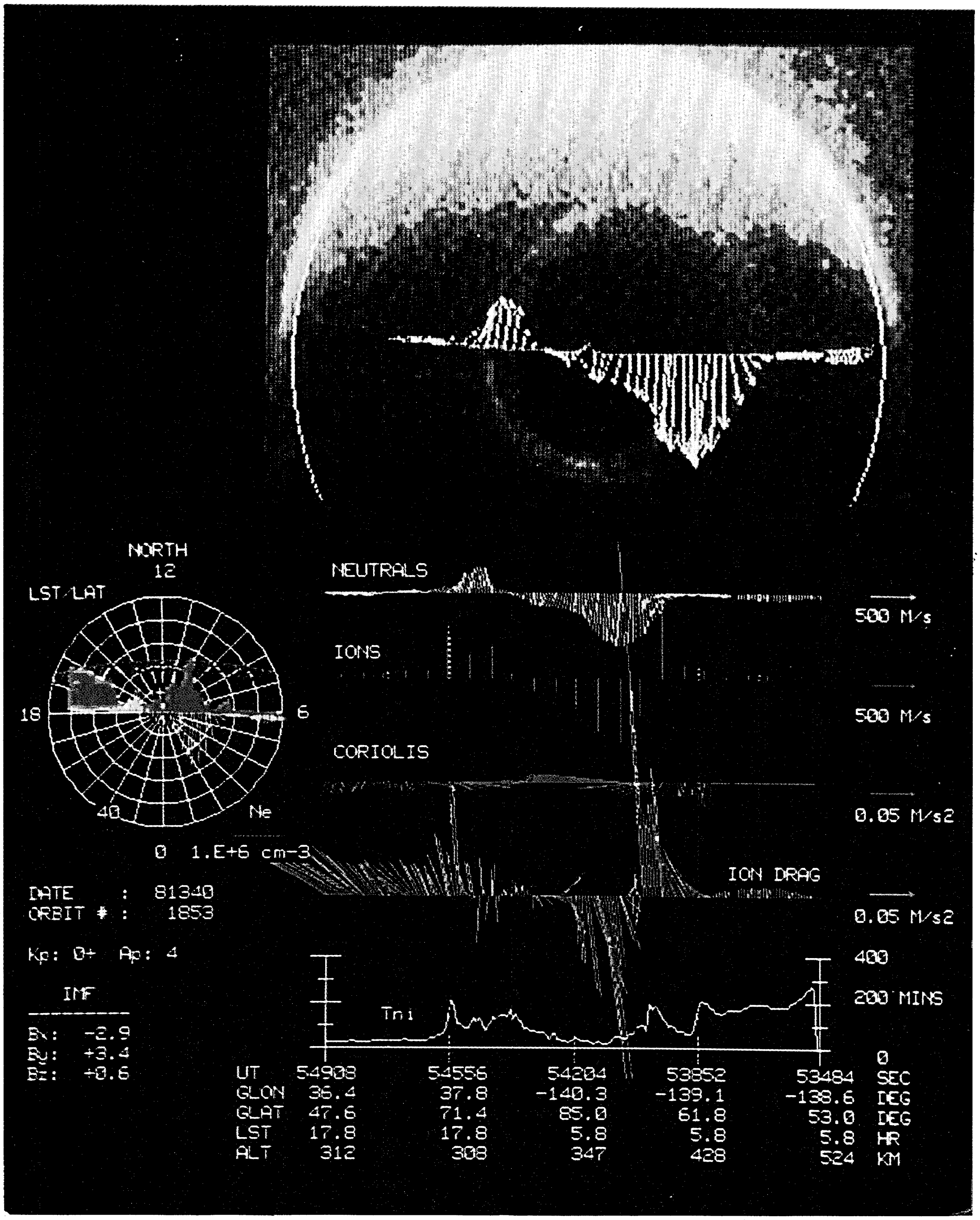

FIGURE 7. A detailed study of the situation shown in figure 6*a* (Killeen *et al.* 1988); day 340, 1981, orbit 1853. Properties of the thermal plasma (ion density and ion drift) within the polar region are shown, along with a determination of the ion–neutral collision time constant, T_{ni}, and various important forces coupling the high-latitude ionosphere and thermosphere. K_p is 0^+; the IMF is $\boldsymbol{B}$ = (−2.9, + 3.4, + 0.6).

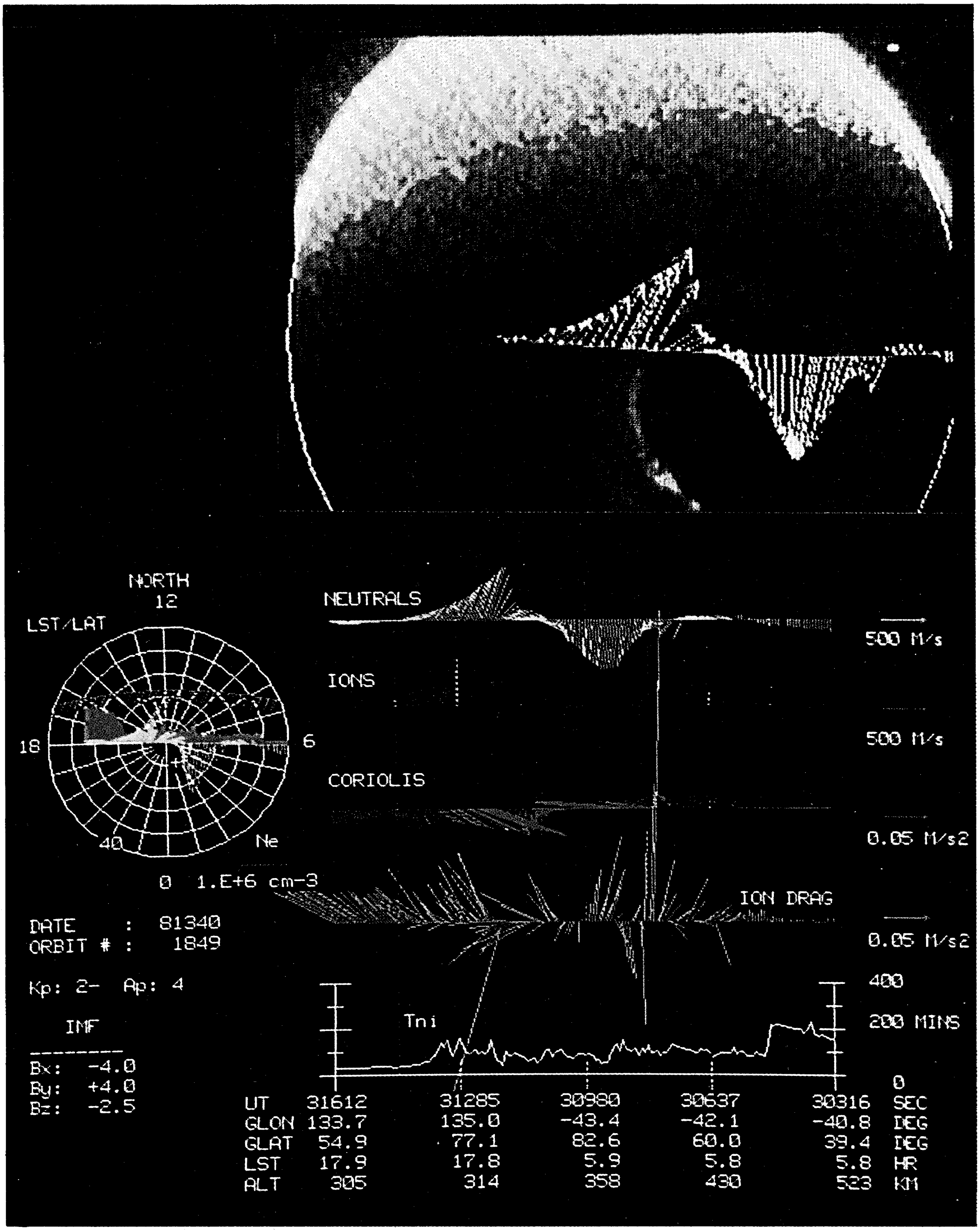

FIGURE 8. Polar dial plot of EISCAT data for 3–4 February 1984 on azimuth 1 (332°), in the same format as figure 3.

component equivalent to the ion velocity perpendicular to the satellite track (zonal component), while LAPI provides thermal plasma density, shown in the section at left. The thermal plasma density is further used to calculate the ion–neutral frictional coupling time constant, which is shown in the lowest panel of figures 7 and 8.

Figure 7 shows the interval (*DE*2 orbit 1853) when B_Z was directed northward. At this time, the northern polar cap is also displaced sunward to almost its maximum extent during the day. Polar cap plasma densities are thus high on the dawn side of the polar cap where, resulting from photoionization and strong plasma transport, a tongue of high ionization density is carried antisunward. This feature is discussed by Fuller-Rowell *et al.* (1988), who show that this plasma tongue is a consistent feature of the modelled polar cap plasma density distribution during the winter period. For several hours either side of 18h U.T., when the IMF B_Y component is positive, there is strong direct plasma transport from the sunlit polar cusp region antisunward on the dawn side of the polar cap. On the dusk side of the polar cap, plasma densities are low, as the result of sunward transport from the nightside, combined with the absence of photoionization and weak precipitation in this part of the polar cap. Heppner & Maynard (1987) describe the polar convection under these conditions (IMF B_Z positive) as a highly distorted two-cell vortex pattern, rather than a multicell system. It is of considerable interest and importance that in the region of intense antisunward flow, the plasma densities are also high, so that the neutral–ion time constant is quite low (10 min or less). The neutral flow on the dawn side of the polar cap thus matches the ion flow quite accurately, whereas in the dusk auroral oval, the dusk part of the polar cap, and the dawn auroral oval, the plasma density is much lower, the neutral–ion time constant is around 3 h, and neutral flows are much weaker than the ion flows. For example, the winds do not turn sunward in the dawn auroral oval, despite sunward ion flows of 600–800 m s^{-1}.

In figure 8, the comparable set of data for *DE*2 orbit 1849 are shown. At this time, the geomagnetic polar cap is located further towards the nightside, and the polar cusp is not in direct sunlight.

Although there is also a strong antisunward plasma flow within the polar cap, the plasma densities are considerably reduced compared with those shown in figure 7. The peak antisunward winds are 60%, rather than 90% of the ion flow speed, consistent with a longer time constant of ion–neutral momentum coupling (lower polar cap and auroral oval plasma densities, as shown in the left-hand element of the figure). This polar cap plasma behaviour is fairly typical of the U.T. period when the geomagnetic polar cap is displaced away from the Sun near the winter solstice, and the supply of high-density plasma to the cusp region is cut off. In the dusk auroral oval, the sunward winds are much stronger than those shown in figure 7 (which were actually obtained 6 h following the observations shown in figure 8).

Other observations from *DE*2 which have proved to be extremely valuable for interpreting the state of the thermosphere have been obtained from the neutral atmosphere composition sensor (NACS, Carignan *et al.* 1981). This instrument, particularly in combination with the combined FPI and WATS wind data, has provided an invaluable insight into the real workings of the so-called 'wind diffusion' mechanism. Briefly, sustained large-scale advective horizontal wind flows, combined with vertical upwelling, in regions of strong and sustained heating, with a lower altitude (and lower velocity return flow) cause a breakdown of static diffusive equilibrium (Mayr & Volland 1972). As a result, regions of sustained heating are characterized, at F-region altitudes, with an excess of heavy molecular species, compared with that anticipated considering the gas temperature, and using a solution assuming static diffusive equilibrium. Conversely, in regions of sustained downwelling, there should be a relative reduction of the heavy molecular species, and a corresponding decrease in the mean molecular mass.

In figure 9, a systematic analysis of *DE*2 WATS, FPI and NACS data during October 1981 shows how closely geomagnetic processes control thermospheric temperature, composition and wind velocity in the Southern (summer) Hemisphere. *DE*2 was in the 22.8–08.6h LT plane during this period. The combination of high solar insolation and geomagnetic heating and momentum transfer not only forces a characteristic high-latitude wind pattern throughout the middle and upper thermosphere, but also dominates the neutral gas temperature and composition. This presentation (taken from Rees *et al.* 1985) plots the neutral temperature and wind, mean molecular mass, atomic oxygen density and molecular nitrogen density as functions of U.T. and true anomaly (essentially colatitude is displayed, with the southern polar crossings across the centre of each section of the figure). This presentation is possible because *DE*2 was in a polar orbit of relatively low eccentricity. Throughout the U.T. day, the Earth rotates underneath the satellite orbit. The horizontal axis can therefore be thought of as either U.T., or else, for a limited period, geographic longitude. The sinusoidal curve represents the closest approach of the satellite, each orbit, to the southern geomagnetic pole.

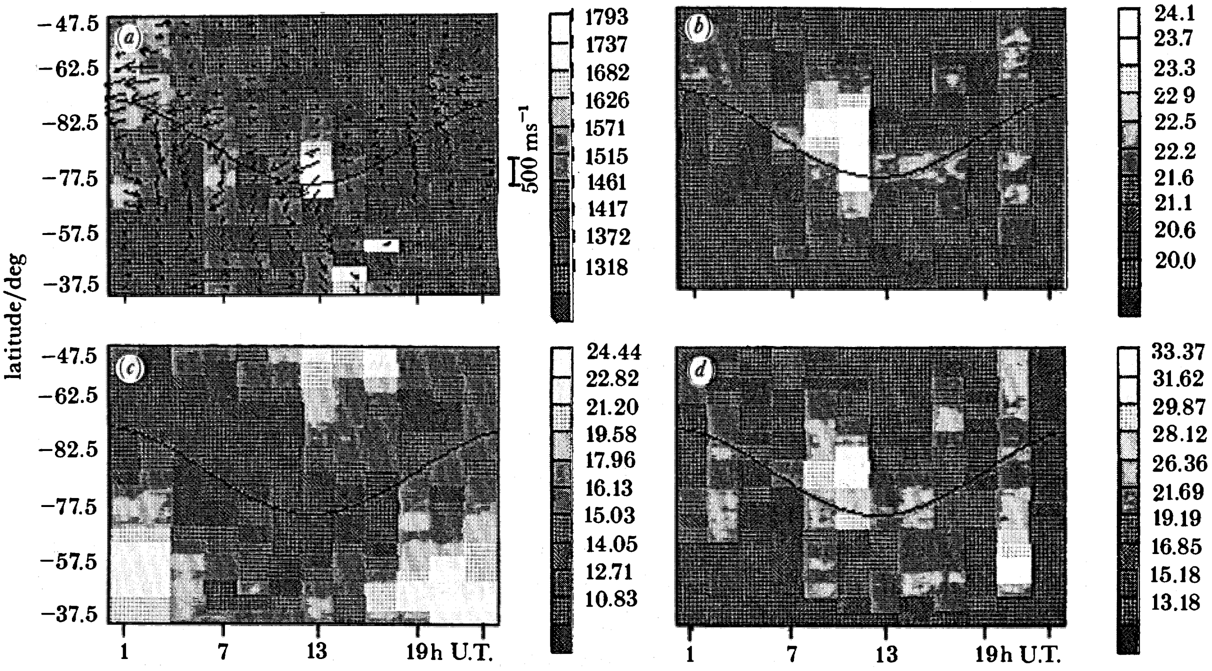

FIGURE 9. Statistical distributions of neutral composition, wind and temperature for the south polar region during October 1981 as observed by *DE*2 in the 22.8–08.6h LT orbit plane. (*a*) Temperature plot (in kelvins); (*b*) molecular mass (in unified atomic mass units); (*c*) O_2 density and (*d*) N_2+O_2 density plots (in units of 10^{-12} kg m^{-3}).

There is a close relationship between the vicinity of the geomagnetic pole and the regions where the largest compositional disturbances are routinely found. The geomagnetic signature is therefore one of strongly increased wind, temperature, mean molecular mass, decreased atomic oxygen (and helium) densities, and strongly increased molecular nitrogen density (also argon). This is a profound composition change, not merely a raising of constant pressure surfaces due to the temperature increase. The convective overturning causes a compositional change much larger than that which would be caused purely by a vertical expansion of the atmosphere.

Rees *et al.* (1985) discuss in some detail a comparison between two sets of *DE2* data, one from the Northern Hemisphere obtained during December 1981 and the second obtained in the Southern Hemisphere in October 1981. They used a number of model simulations which were generated specially to investigate the major terms causing the observed thermospheric structures in neutral thermospheric temperature and wind velocities in the winter and summer geomagnetic polar regions. In December 1981, *DE2* was in the 18–06h LT time plane. Wind, temperature and composition patterns within the polar regions display complex structures as functions of latitude and U.T. The highest wind velocities, and strong enhancements of temperature and of mean molecular mass closely follow the latitudinal variation (displayed as true anomaly) of the geomagnetic polar region. These statistical studies confirm that there are strong antisunward flows over the central polar cap, strong sunward flows in the dusk auroral oval, and just a reduction of the low-latitude antisunward flow in the location of the dawn auroral oval, complementing the impression from the data from a small number of individual orbits discussed earlier, and by Hays *et al.* (1984).

4. MODEL SIMULATIONS

The following section will present results from a series of numerical simulations of the UCL thermospheric GCM or the version coupled with the Sheffield ionospheric model code. Most of the observational data can be understood and interpreted within the context of the model.

4.1. *Global temperature and composition structure*

To place the high-latitude data in context, it is useful to first consider the global structure of temperature and composition, and it is this question that can be addressed first by the model. The global distributions have become well established by the observational data and are incorporated in the recent empirical models of the thermosphere. The model simulations can then be used to examine, and perhaps confirm or extend theories of the causes of the thermospheric patterns. Often, such comparisons between theoretical models and data highlight new possibilities.

Figure 10 illustrates the global distributions of temperature, mean molecular mass, atomic oxygen and molecular nitrogen concentrations in the upper thermosphere as simulated for conditions of moderate solar activity and low geomagnetic activity, at the December solstice. The region from the north to the south geographic pole is illustrated at pressure level 12 close to 300 km altitude. Two features are immediately apparent. Firstly, there is a strong diurnal response of thermospheric temperature, particularly at low and middle latitudes, to the solar forcing, a factor which is unique to the upper atmosphere. Secondly, there is a strong latitudinal gradient of temperature, decreasing from the summer polar regions to the winter polar region. For this situation of low geomagnetic activity, the high-latitude 'geomagnetic' sources are fairly weak and are only apparent in the slightly enhanced wind magnitudes within the polar regions. The global circulation responds to the latitudinal temperature, and related pressure, gradients. There is a mean wind circulation at upper thermospheric altitudes flowing

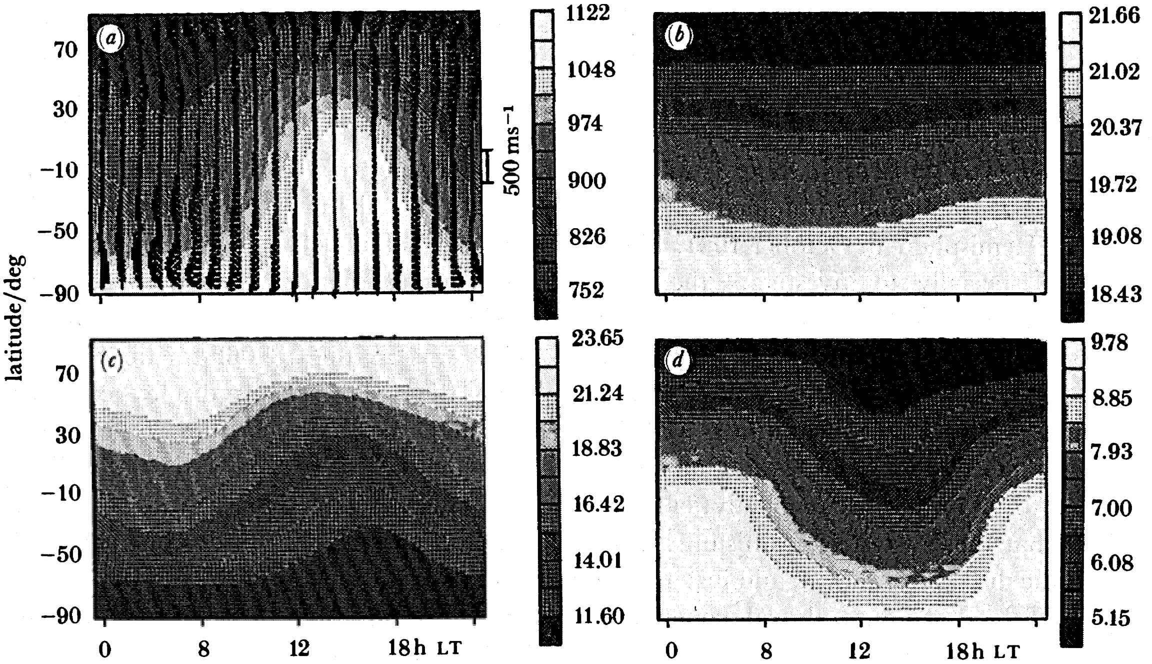

FIGURE 10. Simulation (three-dimensional coupled model) of neutral composition, wind and temperature in December, for pressure level 12 (*ca.* 300 km), at 18h U.T. and high solar activity ($F_{10.7} = 185$) and low geomagnetic activity. (*a*) Temperature plot (in kelvins); (*b*) molecular mass (in unified atomic mass units); (*c*) O_2 density and (*d*) $N_2 + O_2$ density plots (in units of 10^{-13} kg m^{-3}).

from the summer to winter hemisphere, and a weak return flow in the lower thermosphere–mesosphere. This interhemispheric horizontal flow creates a region of upwelling at summer high latitudes and downwelling at winter high latitudes. The compositional structure is a direct consequence of this global circulation cell. When part of a large-scale combined convective and advective overturning régime, the concentrations of heavy molecular species are enhanced relative to light atomic species in regions of upwelling, while in the regions of downwelling, the ratio of heavy molecular to light atomic species is decreased.

In the simulations, geomagnetic activity is increased by increasing the magnitude of the polar convective electric field and corresponding intensity of particle precipitation at high latitudes. The global structure of the thermosphere and ionosphere is thus modified. Figure 11 shows the same four parameters for the same season and solar activity, but for a level of moderately high geomagnetic activity, equivalent to a situation when K_p would be steady about 3 to 3^+. The increased geomagnetic input strengthens the polar winds and heats the polar regions. As a result the global pressure gradients are modified, as are the wind cells. The circulation from summer to winter pole is stronger, but no longer quite extends to the winter pole. A cell of opposing circulation has developed between the winter pole and high winter mid-latitudes, reversing the prevailing wind. This circulation change also alters the compositional response. The lowest values of mean molecular mass are now found at high winter mid-latitudes and a second region of high values of mean molecular mass is present near the winter pole, in response to the upwelling caused by the increased geomagnetic input.

As the level of geomagnetic activity increases further, some of the causes of the extreme neutral wind observations discussed previously become apparent. Figure 12 illustrates the neutral wind and temperature distributions following a period where the K_p would have been

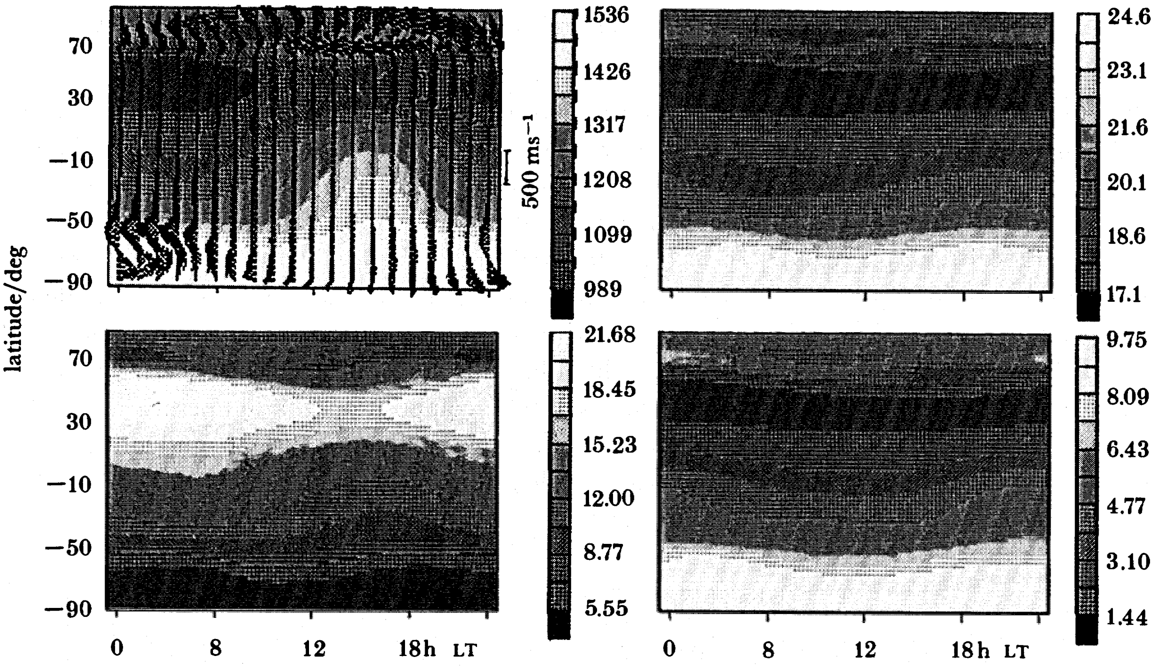

FIGURE 11. Model simulation of neutral composition, winds and temperature in December, for pressure level 12 (*ca.* 300 km), at 18h U.T. and high solar activity and moderate geomagnetic activity (K_p of 3^+). (*a*) Temperature plot (in kelvins); (*b*) molecular mass (in unified atomic mass units); (*c*) O_2 density and (*d*) N_2+O_2 density plots (in units of 10^{-12} kg m^{-3}).

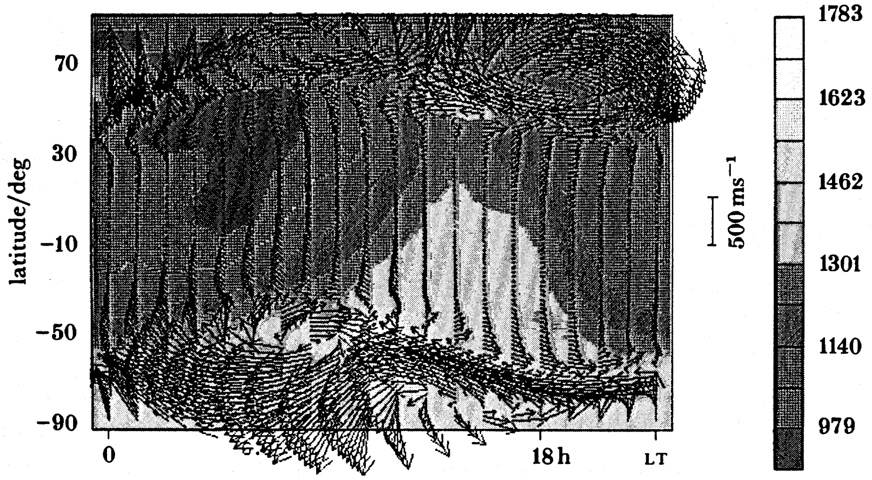

FIGURE 12. Model simulation of neutral composition, winds and temperature (in kelvins) in December, for pressure level 12 (*ca.* 300 km), at 0h U.T. and high solar activity ($F_{10.7}$ = 185) after a period of very high geomagnetic activity.

around 7 for about 6 h. Neutral winds approaching 1 km s^{-1} are generated, with a particularly strong response in the dusk auroral oval (sunward winds) and over the polar cap (antisunward winds). These are particular features seen in the ground-based and satellite observations during very disturbed periods. Even in the dawn auroral oval, sunward winds of nearly 300 m s^{-1} are generated. Such strong eastward winds are rather rare, although still less than the 600–700 m s^{-1} observed on 12 February 1982 from Kiruna.

4.2. *Seasonal and* IMF-B_Y *control of the high-latitude composition and plasma density*

The geomagnetic control of the thermospheric composition at high latitudes was illustrated in figure 9. Figure 13 shows a model simulation for a similar period, corresponding to October 1981, when solar activity was very high. The average geomagnetic activity was also high. The neutral temperature, mean molecular mass, atomic oxygen density and molecular nitrogen density are presented as a function of U.T. and colatitude, as it would be sampled by a satellite in a fixed local-time plane, 09–21h LT, at 320 km altitude, essentially an equivalent format to that displayed in figure 9. Both the average values and the structure of the modelled composition data are in excellent agreement with the FPI, WATS and NACS measurements, and clearly illustrate the cause of the observed high-latitude structures to be associated with the geomagnetic polar region. Major disturbances in both composition and temperature response follow closely the location of the geomagnetic polar cap as a function of U.T. and latitude (the satellite's closest approach to the geomagnetic pole is illustrated by the sinusoidal curve). The general agreement is good both quantitatively as well as qualitatively.

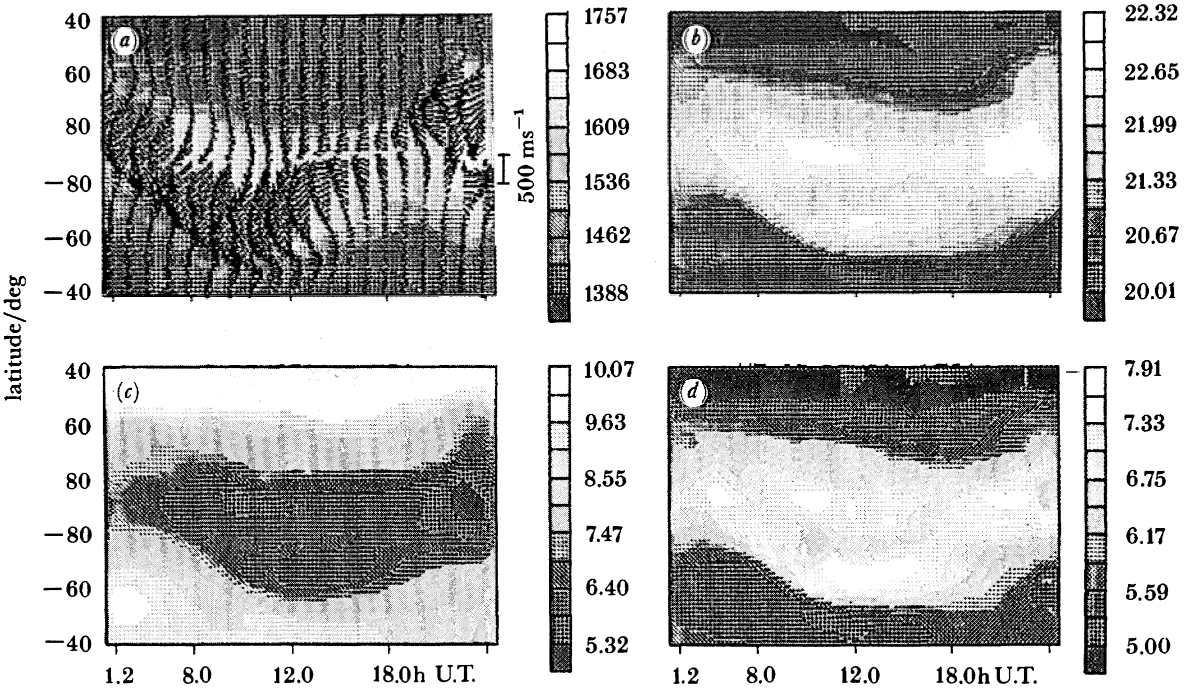

FIGURE 13. Neutral composition, winds and temperature for the south polar region during October 1981 in the 09–21h LT plane, as simulated by the thermospheric model (presented in the same format as figure 9). (*a*) Temperature plot (in kelvins); (*b*) molecular mass (in unified atomic mass units); (*c*) O_2 density and (*d*) N_2+O_2 density plots (in units of 10^{-13} kg m^{-3}).

To illustrate the thermospheric and ionospheric response at high-latitudes to the orientation of the B_Y component of the IMF in summer and winter we will use data from four simulations of the UCL–Sheffield coupled model. These simulations have been generated for IMF B_Z negative (southward), and for conditions when the IMF B_Y component was either strongly positive, or strongly negative, for a geomagnetic activity level corresponding to an approximate K_p value of 3–4, and for moderately high solar activity ($F_{10.7} = 185$). Two of the simulations are for the December solstice and two for June. The simulations are time-dependent, that is they are U.T.-dependent, and the results are diurnally reproducible. However, the external solar and geomagnetic inputs are time-independent. These four simulations use an offset dipole representation of the geomagnetic field.

The characteristic U.T. variations of the summer and winter polar regions are dependent on the offset of the geomagnetic poles from the geographic poles. During the U.T. day, at all seasons, the geomagnetic polar caps are carried into and out of sunlight. There is, therefore, a large diurnal modulation of the solar photoionization and UV or EUV heating of the geomagnetic polar regions which also causes large U.T. variations in plasma density, conductivity, ion drag and Joule and solar heating of the polar thermosphere. There are consequent large U.T. modulations of the thermospheric and ionospheric response. These characteristic U.T. variations of thermospheric and ionospheric structures, and the associated thermospheric–ionospheric interactions are discussed by Fuller-Rowell *et al.* (1988).

In this paper we will select the 18 U.T. period to illustrate the response of neutral wind, composition, and plasma density to the orientation of IMF-B_Y, in summer and winter, and to illustrate the coupling between these parameters. Figure 14 is a montage of four polar plots

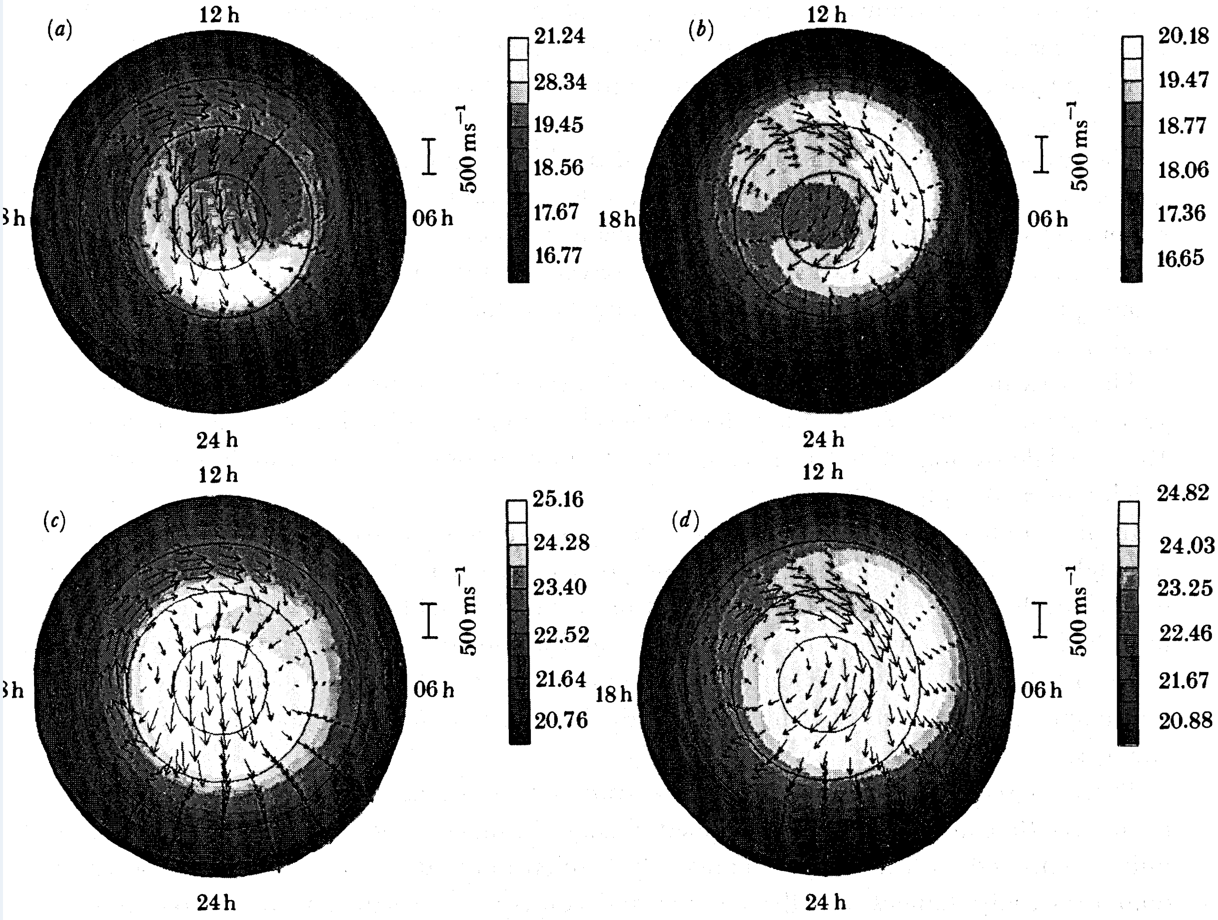

FIGURE 14. A montage of four plots, 50–90° latitude, of mean molecular mass (in unified atomic units) and neutral wind from the coupled model at pressure level 12, high solar activity ($F_{10.7} = 185$) and moderate geomagnetic activity (K_p of 3^+). (*a*) Winter B_y negative; (*b*) winter B_y positive; (*c*) summer B_y negative; (*d*) summer B_y positive. All at 18h U.T.

from 50–90° geographic latitude for the Northern Hemisphere. Mean molecular mass is shown at pressure level 12, *ca.* 300 km altitude, together with the neutral wind vectors. The winter simulations of B_Y negative and positive are shown in figure 14*a*, *b* respectively, and summer solstice conditions are shown in figure 14*c*, *d* for B_Y negative and positive respectively.

At F-region altitudes, only relatively small differences in the wind patterns can be ascribed to seasonal effects. In the winter, the winds in the dawn auroral oval show only a slight tendency to follow the relatively weak sunward ion convection (B_Y positive). In the summer, there is no significant indication of sunward wind acceleration at all in the dawn cell for B_Y positive. Only minor seasonal differences occur in the strong clockwise circulation wind cell which follows the strong sunward ion convection in the dusk auroral oval and antisunward ion flow over the dawn side of the polar cap. Equatorward of the nightside auroral oval, the wind flow is distinctly equatorward in the June simulation, and rather weaker in the December simulation (100 rather than 200 m s^{-1}).

The B_Y dependence of the neutral wind response therefore is clear for either season. The most distinct effect is that the location of the peak antisunward flow moves from the dawn to the dusk side of the polar cap as the IMF-B_Y changes from positive to negative. In the auroral dawn oval there is a weak sunward wind when B_Y is negative, while for B_Y positive, there is only a reduction of the antisunward wind. In the dusk auroral oval again the sunward winds are stronger for the negative B_Y orientation. The polar neutral winds observed by the *DE* satellite which are presented in the previous figures agree well with the predictions of the model for the different orientations of B_Y.

The highest values of mean molecular mass which occur poleward of 50° latitude in the winter polar F-region are about equal to the lowest value in the equivalent summer polar region. At high winter mid-latitudes, the mean molecular mass is close to 16, indicating a composition which is nearly pure atomic oxygen. There is then a plateau covering the geomagnetic polar region, due to heating and associated upwelling and outflow, where the mean molecular mass reaches 20.

This plateau value of mean molecular mass in the winter polar region is very dependent on geomagnetic activity. At very low activity levels the mean molecular mass may be as low as 16–17, while during extended geomagnetic storm conditions the mean molecular mass may reach values as high as 22.

In the summer polar cap, the lowest values of mean molecular mass above 50° are 20, and the highest values, within the geomagnetic polar cap, reach 24–25. At this constant pressure level (12), this implies a four-fold reduction in the amount of atomic oxygen being transported from high summer mid-latitudes to the pole, and atomic oxygen concentrations which are a factor of 10 lower than those found in the high winter mid-latitude region. The variation of molecular nitrogen density is in direct antiphase, and compensates for the atomic oxygen changes.

There are significant changes in the compositional variations caused by changes in the sense of the IMF B_Y component. These detailed changes in mean molecular mass are modest (1–2 units) compared with the larger changes (3–4 units) induced by the combination of seasonal solar insolation changes and the heating and consequent overturning of the thermosphere resulting from geomagnetic forcing. However, the F-region plasma density is highly responsive to the B_Y-induced compositional modulation. For both seasons, B_Y positive produces peak mean mass values on the dawn side of the polar cap, a product of both the vertical and horizontal transport by the neutral wind field. For B_Y negative, the peak values occur more toward the centre or dusk side of the polar cap. We shall see in the following figure how the B_Y dependent composition structure feeds back into the plasma density distribution in the summer polar cap, where the mean molecular mass is particularly high.

Figure 15 is the equivalent montage of polar plots of plasma density. Figure 15*a* is for winter and B_Y negative; 15*b* for winter B_Y positive; 15*c* for summer B_Y negative; and 15*d* is for summer B_Y positive. The winter high-latitude plasma densities exceed those of the equivalent sunlit summer region, creating an apparent high-latitude ionospheric winter anomaly. Peak densities in the winter sunlit cusp region (which is just in sunlight at 18h U.T.) are about a factor of 2–3 higher than the equivalent summer region.

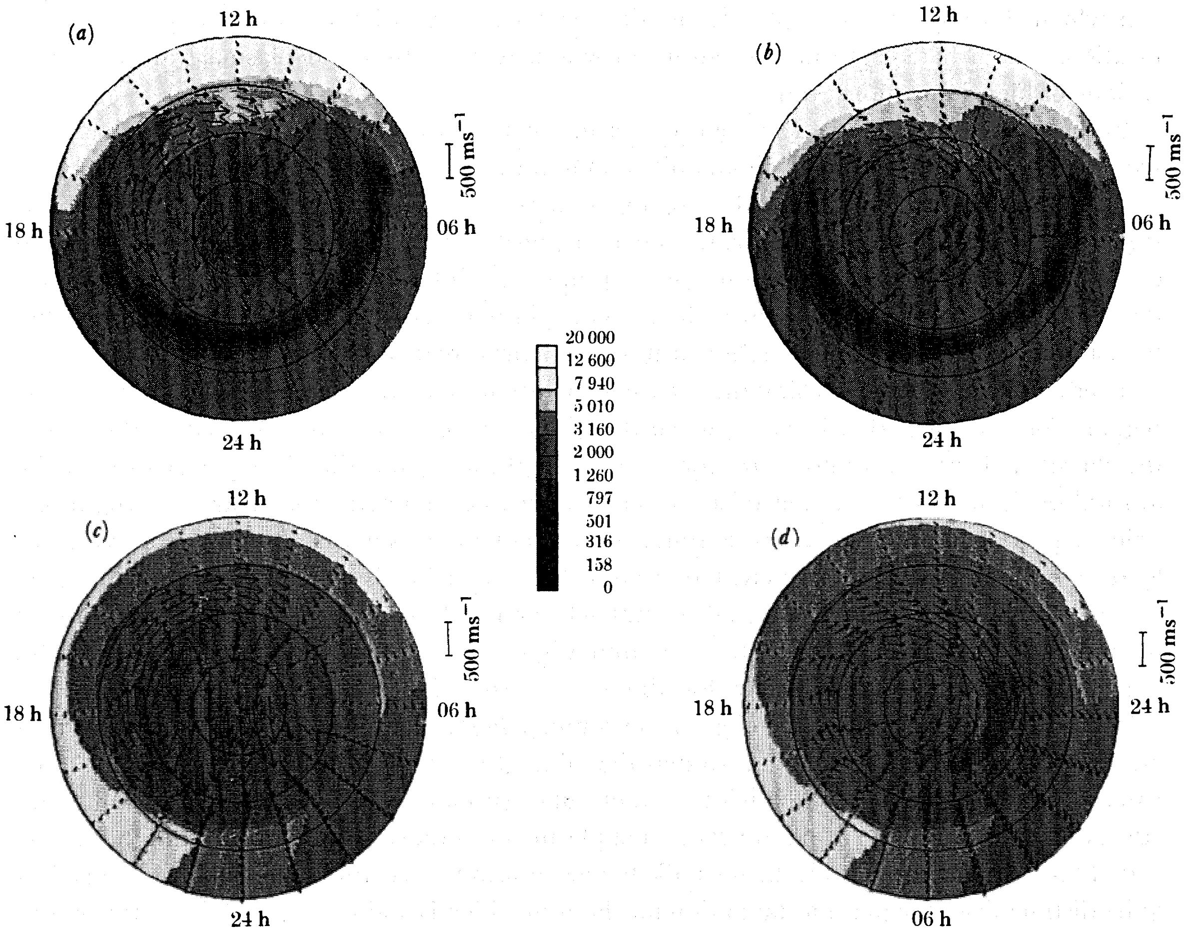

FIGURE 15. A montage of four plots, 50–90° latitude, of ion density (in units of 10^8 m^{-3}) and neutral wind from the coupled model at pressure level 12, high solar activity ($F_{10.7} = 185$) and moderate geomagnetic activity (K_p of 3^+). (*a*) Winter B_y negative; (*b*) winter B_y positive; (*c*) summer B_y negative; (*d*) summer B_y positive.

At 18h U.T., the winter polar cap is filled with high density plasma which has been rapidly convected from the dayside, through the cusp region. For B_Y negative, the ionization tongue extends on the dusk side of the polar cap while, for B_Y positive, it extends over the central region, due to competing magnetospheric convection and corotation. There is a well-developed subauroral trough, from 16 to 08h LT at this U.T. (but which encircles the entire auroral oval near the winter solstice for much of the rest of the U.T. day). At U.T. times when the cusp is not in sunlight, and the antisunward transport of plasma from the sunlit dayside is cut off, the plasma density within the polar cap falls to significantly lower values (Fuller-Rowell *et al.* 1988).

In contrast, the summer sunlit polar cap is a region where the electron recombination rate is high, so that plasma densities are low despite the combination of photoionization and electron precipitation. Regions of lowest plasma density have a one-to-one relation with regions of the highest mean molecular mass. The regions of lowest plasma density within the summer polar cap are responsive to thermospheric compositional changes, induced by convection and advection driven by solar and Joule heating. The details of these responses are highly sensitive to the convection response to IMF-B_Y changes. Regions within the summer polar cap which develop very low plasma densities can be seen to be approximately those same locations which had peaks in ion density in winter, caused by rapid plasma transport from regions of high ionization rates.

In the summer polar region, there is no feature which corresponds to the winter subauroral trough. There is sufficient solar photoionization in the subauroral regions (at least at 18h U.T.) so that subauroral troughs do not develop in regions of plasma stagnation (which are otherwise similar to those of the equivalent winter polar regions). There is enhanced plasma destruction compared with the equivalent winter regions, but the winter values of mean molecular mass (20–21) in those regions do not cause the extreme plasma destruction rates which occur within the summer polar cap, where the mean molecular mass reaches 24–25.

There is one caveat concerning this overall conclusion, related to the southern summer polar region. For a small period in U.T., when the geomagnetic polar cap is rotated furthest from the dayside, there is no photoionization on the nightside, immediately equatorward of the auroral oval, due to the greater offset of the southern geomagnetic pole from the geographic pole. A partial summer subauroral trough may occur under such conditions. However, this feature will never develop to the extent seen in the winter hemisphere. For most of the U.T. day in winter, the subauroral trough completely or nearly completely encircles the auroral oval. At 18h U.T., as depicted in all these simulations, the winter northern polar cusp is sunlit. However, this situation only occurs for about 6 h during the U.T. day.

Subauroral troughs which develop in the summer hemisphere are likely to be the fossils of an earlier, expanded, auroral oval (so that the midnight part of the auroral oval is not sunlit). Intense heating, forcing enrichment of molecular species by convective overturning and advection will lead to the rapid destruction of plasma once the auroral source diminishes at the end of the disturbance. This is the most likely mechanism for creating such troughs, and is thus quite distinct from the plasma stagnation mechanism which is mainly responsible for the winter subauroral trough.

4.3. *Equinox simulation*

Results from a simulation generated for equinox conditions by using the latest version of the UCL–Sheffield coupled model will also be discussed. This simulation has been generated for IMF B_Z negative (southward), and for $B_Y = 0$ conditions, for a geomagnetic activity level corresponding to approximately $K_p = 3$–4, and for low solar activity ($F_{10.7\,\mathrm{cm}} = 80$). The simulation is time-dependent, that is it is U.T.-dependent, and the results are diurnally reproducible. However, the external solar or geomagnetic inputs are time-independent. The simulation uses the corrected IGRF representation of the geomagnetic field for the mapping of the magnetospheric input.

Figure 16 shows the distributions of ion drifts and ion density for the northern polar regions from 60° latitude to the geographic pole, at 12h U.T., and pressure level 12, close to the *F*2 peak. Plasma transport is still effective, in contrast to the previous simulations for the summer polar cap, but is not as dominating as in the winter case. Plumes of high-density plasma are convected over the central portion of the polar cap, but do not survive to circulate into the auroral ovals, as occurred in winter. Plasma which is convected sunward into the dusk auroral oval is therefore of relatively low-density plasma from the nightside. This creates a trough-like feature on the dayside, which delays the increase of ion density. In the dawn sector, the equivalent 'trough' feature is weaker.

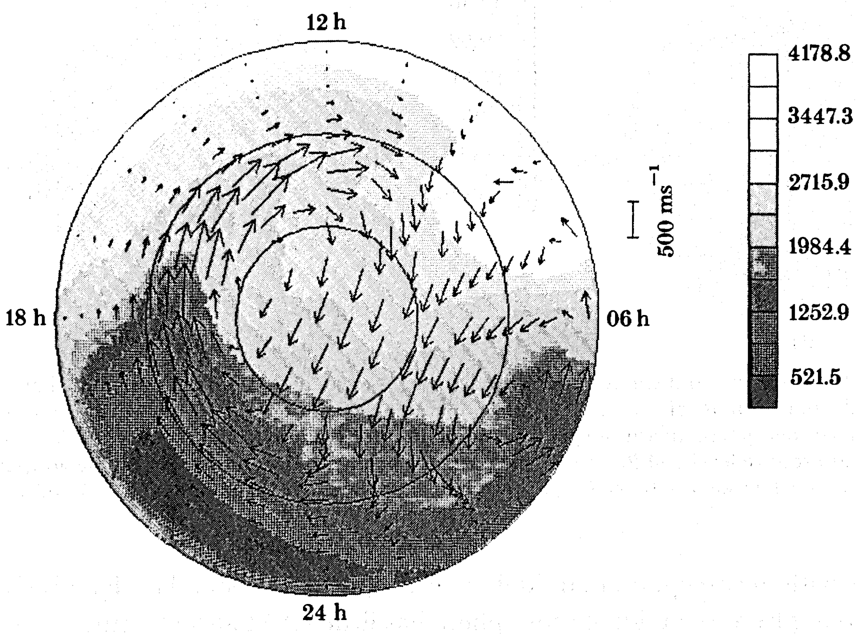

FIGURE 16. Ion density (in units of 10^8 m^{-3}) and ion drifts in the northern polar region, 60–90° latitude, pressure level 12h U.T., close to the F-region peak, at low solar activity ($F_{10.7} = 80$) and moderate geomagnetic activity (K_p of 3^+).

4.4. *Lower thermosphere response*

The response of the lower thermosphere and ionosphere to magnetospheric forcing is as strong and varied as we have seen in the upper thermosphere. It is a region of the neutral atmosphere that has been notoriously difficult to monitor experimentally, although the ISR can probe the plasma environment most effectively. The neutral-wind response to ion-drag forcing and to heating is typically weaker in magnitude than at higher altitudes, due to the greater inertia. At the pressure level (7, *ca.* 120 km), which we will consider, winds are roughly 50% of those in the upper thermosphere, and are also rotated in direction. This is due to the different balances of Coriolis, pressure gradient, and ion-drag forces. Solar heating and tidal forcing from the lower atmosphere are also important, particularly during the quiet geomagnetic periods.

Figure 17 shows the neutral wind, temperature, mean molecular mass, vertical wind, and ion density at pressure level 7, near 120 km, from 50 to 90° latitude, for the same conditions as used

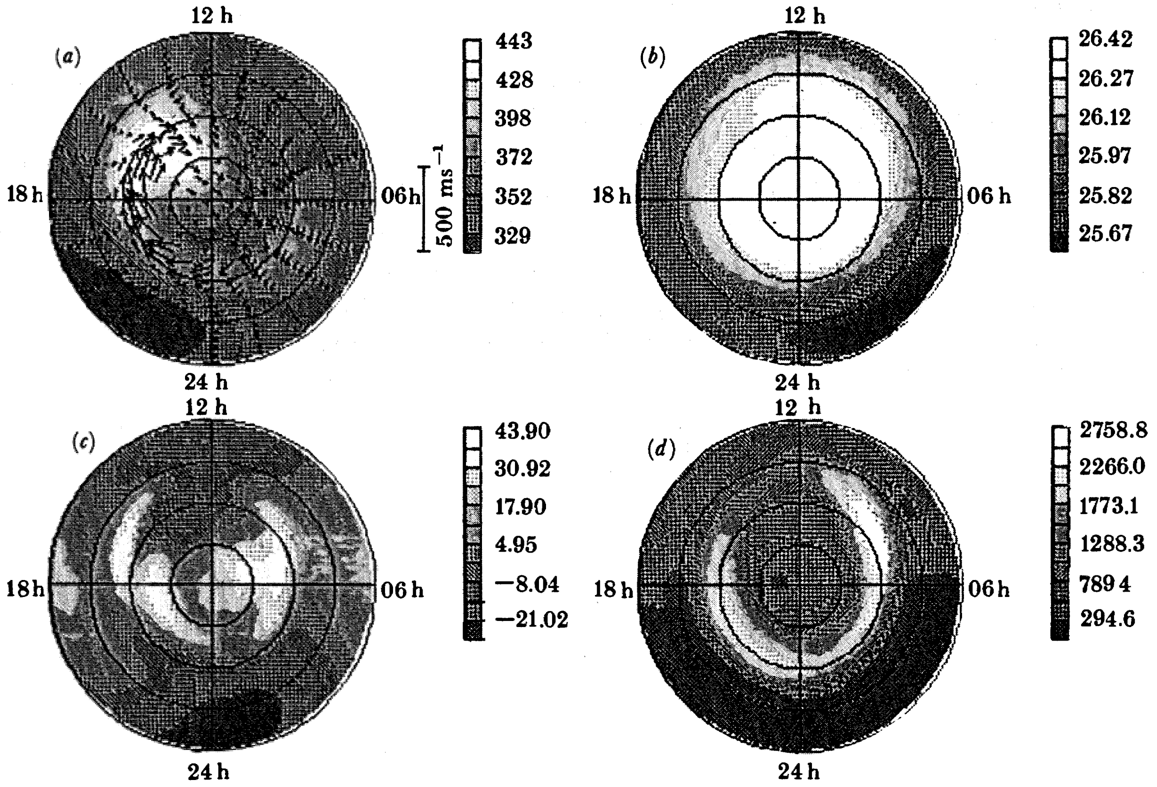

FIGURE 17. (*a*) Wind velocity and temperature (in kelvins); (*b*) mean molecular mass (in unified atomic mass units); (*c*) vertical wind (in units of 10^{-2} m s^{-1}); (*d*) plasma density (in units of 10^8 m^{-3}) distributions taken from the UCL coupled ionosphere–thermosphere GCM simulation for equinox conditions for IMF B_y zero. The data are presented at pressure level 7 (120 km) for the northern polar region (poleward of 50° geographic latitude) and at 18h U.T., for low solar activity ($F_{10.7} = 80$) and moderate geomagnetic activity (K_p of 3^+).

for figure 16, with the exception that tidal forcing at the lower boundary has also been imposed. The tidal forcing from the middle atmosphere has little effect at high latitudes for this level of geomagnetic activity, but its influence can be seen in mid-latitude regions, in both the temperature and vertical wind plots, as a semidiurnal variation. The ion density distribution in the auroral oval is dominated by the distribution of auroral (electron) precipitation, which can be seen to have the elliptical mapping from the distortion of the IGRF magnetic field model. Typical E-region ion densities of between 2 and 3×10^{11} occur in the auroral oval. Outside the auroral oval, solar photoionization generates ion densities a factor 5 lower than those in the auroral oval.

A polar plateau of enhanced mean molecular mass, created by the upwelling from geomagnetic heating, just emerges above the background levels. The variation is weak compared with the upper thermosphere and molecular species dominate everywhere, with a mean mass of *ca.* 26 m_u ($m_u = 1.66 \times 10^{-27}$ kg). The winds respond to the ion-drag forcing, creating a dominant clockwise vortex, with peak magnitudes of about 200 m s^{-1}. The wind and temperature structure has a distinctive character and bears little relation to that seen in the upper thermosphere. Vertical winds up to 0.5 m s^{-1} are driven by local Joule heating associated with the auroral oval, together with the component resulting from a divergence of the horizontal wind field.

4.5. *Magnetospheric coupling*

Interactions between the polar ionosphere and the magnetosphere have not been considered in a self-consistent way in these simulations. The magnetosphere is assumed to be a zero-resistance source of the FAC required to match the Pedersen currents produced by the applied potential. The ionospheric conductivity is produced by the combination of auroral precipitation and solar photoionization sources. Thermosphere–ionosphere interactions, including the induced neutral-wind dynamo (which induces a back-EMF), cause considerable modulation of ionospheric electric currents. Most probably, the real magnetosphere is unable to fully sustain the ionospheric–thermospheric feedback without some changes. The external convection electric field and the FAC should respond to the induced-wind dynamo, and to ionospheric current changes as conductivity responds. As these two major features are modulated, it might be expected that the energetic particle populations and perhaps the morphology of the FAC and magnetospheric magnetic field geometry would change significantly.

At the present time it is only possible to consider qualitatively how such changes would occur, and we can also anticipate that as the magnetosphere is somewhat changed, the thermosphere and ionosphere will again respond, in a continuous feedback loop. In the development of the coupled ionospheric–thermospheric model, we experienced this feedback process, and found that it was stable to slowly varying external (magnetospheric) forcing. However, considering the innate instability of many plasma physics processes, we may anticipate that some ionospheric–magnetospheric interactions may be unstable. Certainly, subgrid-mesh processes involve highly unstable interactions between energetic particle precipitation, the ionosphere, counterstreaming plasma populations and the FAC and magnetic field geometry, with characteristic frequencies in the range from quasi-direct-current to many

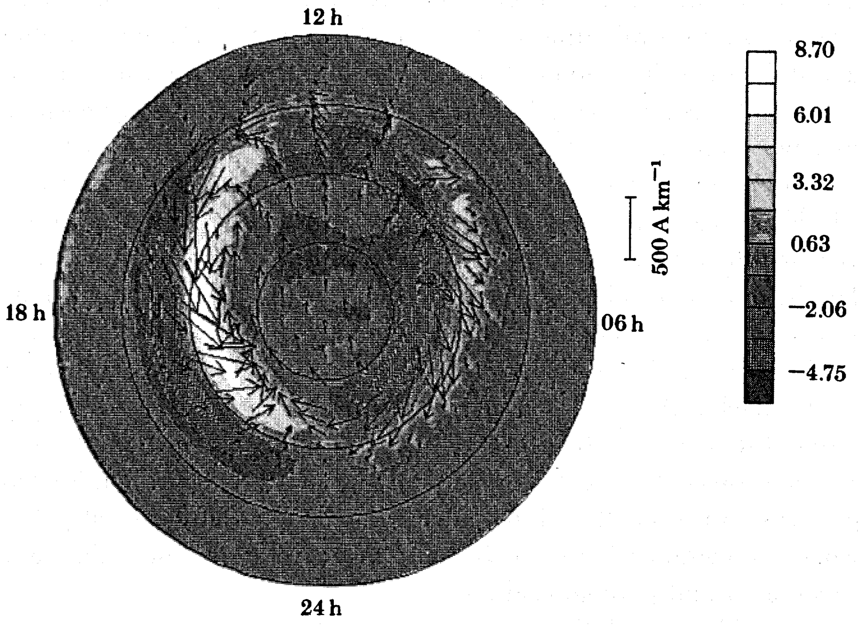

FIGURE 18. The field-aligned current density (in units of 10^{-1} μA m^{-2}) in the high-latitude thermosphere, and the height-integrated current vectors, for the same conditions as figure 17.

megahertz. We may hope at the frequency range required for the model simulations, the magnetospheric–ionospheric feedback is marginally stable, without loss of reality if high frequency and subgrid-mesh processes are initially ignored.

The next major task for the development of these coupled ionosphere–thermosphere models will be the experimental process of attempting to couple into the advanced magnetosphere models. Figure 18 shows the horizontal current density flowing in the northern polar regions for the conditions of Figure 16. Also shown is the FAC pattern. This is derived from the divergence of the horizontal current system, and indicates the current demand on the magnetosphere. Upward current is denoted as positive (light), downward current is negative. The region 1 and region 2 Birkeland currents can be clearly seen in both the dusk and dawn sectors of the auroral oval.

5. SUMMARY

The past decade has seen a major improvement in the quality and quantity of experimental data available to study the thermosphere and ionosphere and their response to magnetospheric forcing. Earlier, large measured changes of individual parameters were difficult to place in a global or large-scale perspective. However, a clear picture of the distinction between the solar and geomagnetic forcing processes has emerged from the combined data-sets available from spacecraft such as the *Dynamics Explorers*, and from ground-based radar and optical observations of the polar thermosphere. A first experimental view of the strong coupling between the thermosphere and ionosphere has also emerged from these combined new data-sets.

In parallel with the development of observing techniques, numerical models of the thermosphere and ionosphere have matured. We are at a state where the combined thermosphere and ionosphere can be modelled self-consistently. We can now realistically simulate the response of the combined system to the magnetospheric forcing, and also investigate the many and varied feedback processes between the two components. The models can be used to understand and interpret the diversity of experimental observations, and provide the framework for evaluating phenomena which are as yet not well understood.

The dominant thermosphere–ionosphere interactions which appear from the modelling studies and which have counterparts in the experimental database can be summarized.

In the winter polar region, ionization enhancements are observed which are due to auroral particle precipitation in both the E-region and in the F-region. The former are relatively easy to understand, since decay rates are generally rapid, and large-scale transport is unimportant. The sole caveat will be related to sporadic-E layers of long-lived metallic ions.

In the polar F-region, neutral winds, neutral composition changes, convection changes and solar photoionization all cause important modifications of plasma distributions. In the winter, plasma convection and winds cause important effects in the horizontal and vertical transport of plasma, respectively. As such, plumes of high density (or low-density) plasma are transported large distances from their origin, and local plasma densities are rarely explicable by local sources and sinks. The exact distributions will depend very much on detailed plasma convection patterns. However, the winter subauroral trough and localized polar troughs will be created when the combination of convection and corotation cause plasma stagnation in regions out of sunlight and photoionization.

There is a strong U.T. modulation of plasma density within the winter polar cap and dusk auroral oval (generally) as the polar cusp enters sunlight for a few hours around 18h U.T., and there is a direct source of high-density plasma (photoionization plus particle ionization) convected through the cusp. At other U.Ts, the source is generally cut off, and polar plasma densities generally decay.

Summer F-region high-latitude and polar plasma densities are generally a factor of about 3–5 lower than in winter. This is due to the seasonal F-region neutral composition variation, generated by summer to winter mean circulation, by which increased plasma recombination rates (due to much higher molecular nitrogen densities) more than compensate for the increased solar photoionization source in the summer polar cap. In turn, this mean circulation is generated by the combination of asymmetric solar insolation and greater geomagnetic heating in the summer compared with winter polar regions (Rees *et al.* 1985, 1987). Particularly at times of high geomagnetic activity, the summer 'F-region' neutral composition is close to that of the standard atmosphere E-region.

The major features of the summer polar F-region are thus quite different to those of the corresponding winter region. Plasma troughs develop in regions of very strong Joule heating, i.e. where ion convection is strongest. As such, the location and intensity of the troughs is quite dependent on the plasma convection patterns. Summer-time troughs tend to occur in the same regions where rapid transport causes high-density plasma plumes in the winter polar region. The classical subauroral trough is distinctly a feature of the winter polar F-region. Even at equinox, the full subauroral trough does not develop, while in winter it fully encircles the geomagnetic polar cap for much of the U.T. day (except around 18h U.T.). In the summer F-region, stagnation troughs do not develop within the polar cap, irrespective of convection pattern. Any polar cap troughs are a result of changes in neutral composition. Subauroral troughs can only develop around the summer polar region when the auroral oval is expanded so that the midnight part of the auroral oval extends into the nightside. Conditions for this situation are likely to occur preferentially in the southern polar region, due to the greater offset of the geomagnetic from geographic pole.

The E-region response to geomagnetic forcing is also strong, although generally rather less marked than in the F-region, in terms of the neutral thermal and compositional response. The major feed-back between the thermosphere and ionosphere occurs due to the effects of high induced winds, since the neutral chemical changes do not significantly affect the ionospheric chemistry. Apart from localized effects such as sporadic-E layers, high-speed auroral oval winds do not cause significant vertical transport of E-region molecular species, due to rapid recombination. The most significant vertical transport effects will be in non-sunlit regions, where ion production is lowest. The dynamo effect of induced E-region winds of 200–400 m s^{-1} is also quite significant. Such winds reduce horizontal currents, with an implication that the FAC or Pedersen currents may also be decreased, with a possible feedback to the convection electric field. There is still relatively little data available for detailed case-study comparisons. Such studies have been quite successful in improving our understanding of the F-region behaviour, and the CEDAR initiative and programmes such as LTCS promise to extend the range of multiparameter data-sets to the E-region as well.

Simulating atmospheric density and compositional structure with numerical models is one of the most testing demands. Density at a given altitude is very sensitive to the total thermospheric energy budget, and is thus liable to be the first casualty of cumulative small errors in the many external terms of the energy input. There are also some indeterminate factors in the radiative energy budget of the lower thermosphere and upper mesosphere. In practice, we have found that the present version of the coupled model computes density and composition relatively accurately, compared with mean mass spectrometer and incoherent scatter (MSIS) predictions for comparable solar and geomagnetic activity levels and for different seasonal conditions. Typical differences (MSIS to model) of around 20% occur at F-region altitudes in the data-sets shown in the model simulations described within this paper. This is roughly comparable with the standard deviation of MSIS in comparison with satellite data-sets for specific locations and times. The numerical models have greater spatial and temporal resolution than MSIS models and relate to real physical processes. Undoubtedly, however, the real thermosphere contains a whole spectrum of high-frequency variations which are beyond present parametrization techniques, our current description of geomagnetic inputs and present computer limitations.

From the initial coupled-model simulations it is possible to examine key features of the coupling between the magnetosphere and the thermosphere–ionosphere. Field-aligned currents reflect the divergence or convergence of the ionospheric Pedersen current. The Pedersen current depends on changes of the ionospheric conductivity and also the dynamo effects of induced winds. Both FAC and E-region winds display considerable seasonal, U.T. and geomagnetic activity variations. Except in the unlikely event that the magnetosphere acts as a 'zero-resistance' source of charge, and momentum, etc., we would anticipate, on the basis of these thermosphere–ionosphere model simulations, to see corresponding modulation of magnetosphere–ionosphere forcing as a function of U.T., season and geomagnetic activity. However, a detailed theoretical evaluation of such processes will have to await the development of a new range of coupled models embracing the near-Earth environment.

As new experimental data from coordinated ground-based campaigns becomes available over the next several years, and it is to be hoped from new space missions within the next decade, we may hope that the validity of many of the simplified assumptions we currently have to make within present models can be tested. Undoubtedly, many present concepts will be found wanting. The impact of global images of particle precipitation and energy deposition, coupled with perhaps the development of techniques of imaging polar plasma convection patterns will mean that future models are capable of looking at the effects of short period and smaller-scale variations in forcing. The present patterns of magnetospheric forcing are too simplified and averaged in time and space. While the thermosphere averages out rapid and short-scale momentum inputs, the energy input integrates all variations, including the effect of rapid forcing variations. The thermospheric composition responds to this 'additional' energy source in a way which presently cannot be simulated accurately, and we already know how sensitive the polar plasma environment appears to be to thermospheric composition changes forced by the combined solar and magnetospheric forcing.

We are indebted to Dr Fred Rich for provision of the Heppner & Maynard polar electric fields in the form of harmonic coefficients. We also thank John Harmer and Hilary Hughes for their assistance in preparing, running and processing the computer simulations using the UCL–Sheffield coupled ionospheric–thermospheric model. Computer time was made available by the University of London Computer Centre (CRAY 1-S) and on the CRAY-XMP-48 at the Rutherford Appleton Laboratory (Science and Engineering Research Council). The research was supported by grants from the U.K. SERC, and from the European Office of Aerospace Research and Development (AFOSR-86-341). The IGRF magnetic field model was provided, in computer-readable form, by the British Geological Survey, Edinburgh.

REFERENCES

Alcayde, D. & Fontanari, J. 1986 Neutral temperature and winds from EISCAT CP-3 observations. *J. atmos. terr. Phys.* **48**, 931–947.

Alcayde, D., Caudal, G. & Fontanari, J. 1986 Convection electric fields and electrostatic potential over 61° < Λ < 72° invariant latitude observed with the European incoherent scatter facility. 1. Initial results. *J. geophys. Res.* **91**, 233–247.

Allen, B. T., Bailey, G. J. & Moffett, R. J. 1986 Ion distributions in the high-latitude topside ionosphere. *Annls Geophysicae* A **4**, 97–106.

Armstrong, E. B. 1969 Doppler shifts in the wavelength of the OI 6300 line in the night airglow. *Planet. Space Sci.* **17**, 957–974.

Banks, P. M. & Kockarts, G. 1973 *Aeronomy*. New York: Academic Press.

Carignan, G. R., Block, B. P., Maurer, J. C., Hedin, A. E., Reber, C. A. & Spencer, N. W. 1981 The neutral mass spectrometer on the *Dynamics Explorer*. *Space Sci. Instrum.* **5**, 429–441.

Cole, K. D. 1962 Joule heating of the upper atmosphere. *Aust. J. Phys.* **15**, 223–235.

Cole, K. D. 1971 Electrodynamic heating and movement of the thermosphere. *Planet. Space Sci.* **19**, 59–75.

Chiu, Y. T. 1975 An improved phenomenological model of ionospheric density. *J. atmos. terr. Phys.* **37**, 1563–1570.

Dickinson, R. E., Ridley, E. C. & Roble, R. G. 1981 A three-dimensional general circulation model of the thermosphere. *J. geophys. Res.* **86**, 1499–1512.

Dickinson, R. E., Ridley, E. C. & Roble, R. G. 1984 Thermospheric general circulation with coupled dynamics and composition. *J. atmos. terr. Phys.* **41**, 205–219.

Fesen, C. G., Dickinson, R. E. & Roble, R. G. 1986 Simulations of the thermospheric tides at equinox with the National Center for Atmospheric Research thermospheric general circulation model. *J. geophys. Res.* **91**, 4471–4489.

Foster, J. C., Holt, J. M., Musgrove, R. G. & Evans, D. S. 1986 Ionospheric convection associated with discrete levels of particle precipitation. *Geophys. Res. Lett.* **13**, 656–659.

Frank, L. A., Craven, J. D., Ackerson, K. L., English, M. R., Eather, R. H. & Carovillano, R. L. 1981 Global auroral imaging instrumentation for the *Dynamics Explorer* mission. *Space Sci. Instrum.* **5**, 369–393.

Fuller-Rowell, T. J. & Rees, D. 1980 A three-dimensional, time-dependent, global model of the thermosphere. *J. atmos. Sci.* **37**, 2545–2567.

Fuller-Rowell, T. J. & Rees, D. 1983 Derivation of a conservative equation for mean molecular weight for a two constituent gas within a three-dimensional, time-dependent model of the thermosphere. *Planet. Space Sci.* **31**, 1209–1222.

Fuller-Rowell, T. J. & Rees, D. 1984 Interpretation of an anticipated long-lived vortex in the lower thermosphere following simulation of an isolated substorm. *Planet. Space Sci.* **32**, 69–85.

Fuller-Rowell, T. J. & Evans, D. S. 1987 Height-integrated Pedersen and Hall conductivity patterns inferred from the *TIROS-NOAA* satellite data. *J. geophys. Res.* **92**, 7606–7618.

Fuller-Rowell, T. J., Rees, D., Quegan, S., Bailey, G. J. & Moffett, R. J. 1984 The effect of realistic conductivities on the high-latitude thermospheric circulation. *Planet. Space Sci.* **32**, 469–480.

Fuller-Rowell, T. J., Rees, D., Quegan, S., Moffett, R. J. & Bailey, G. J. 1987*a* *The thermospheric response and feedback to magnetospheric forcing*. Extended Abstract, Symposium on Quantitative Modeling of Magnetosphere–Ionosphere coupling processes, 9–13 March 1987. Convenors: Y. Kamide & R. A. Wolf. p. 20. Kyoto Sangyo University.

Fuller-Rowell, T. J., Quegan, S., Rees, D., Moffett, R. J. & Bailey, G. J. 1987*b* Interactions between neutral thermospheric composition and the polar ionosphere using a coupled ionosphere–thermosphere model. *J. geophys. Res.* **92**, 7744–7748.

Fuller-Rowell, T. J., Rees, D., Quegan, S., Moffett, R. J. & Bailey, G. J. 1988 Simulations of the seasonal and Universal Time variations of the thermosphere and ionosphere using a coupled, three-dimensional, global model. *Pure appl. Geophys.* **127**, 189–217.

Gustaffson, G. 1970 A revised corrected geomagnetic coordinate system. *Ark. Geophys.* **5**, 595–617.

Hardy, D. A., Gussenhoven, M. S. & Holeman, E. 1985 A statistical model of auroral electron precipitation. *J. geophys. Res.* **90**, 4229–4248.

Harel, M., Wolf, R. A., Reiff, P. H., Spiro, R. W., Burke, W. J., Rich, F. J. & Smiddy, M. 1981 Quantitative simulation of a magnetospheric substorm. 1. Model logic and overview. *J. geophys. Res.* **86**, 2217–2241.

Hays, P. B., Meriwether, J. W. & Roble, R. G. 1979 Nighttime thermospheric winds at high latitudes. *J. geophys. Res.* **84**, 1905–1913.

Hays, P. B., Killeen, T. L. & Kennedy, B. C. 1981 The Fabry-Perot interferometer on *Dynamics Explorer*. *Space Sci. Instrum.* **5**, 395–416.

Hays, P. B., Killeen, T. L., Spencer, N. W., Wharton, L. E., Roble, R. G., Emery, B. A., Fuller-Rowell, T. J., Rees, D., Frank, L. A. & Craven, J. D. 1984 Observations of the dynamics of the polar thermosphere. *J. geophys. Res.* **89**, 5547–5612.

Heelis, R. A., Hanson, W. B., Lippincott, C. R., Zuccaro, D. R., Harmon, L. H., Holt, B. J., Doherty, J. E. & Power, R. A. 1981 The ion drift meter for *Dynamics Explorer-B*. *Space Sci. Instrum.* **5**, 511–521.

Heppner, J. P. 1977 Empirical models of high-latitude electric field. *J. geophys. Res.* **82**, 1115–1125.

Heppner, J. P. & Maynard, N. C. 1987 Empirical high-latitude electric field models. *J. geophys. Res.* **92**, 4467–4490.

Hernandez, G. 1986 *Fabry-Perot interferometers.* Cambridge University Press.

Hernandez, G. & Killeen, T. L. 1987 *Optical measurements of winds and temperatures in the upper atmosphere. CIRA*-87. Oxford: Pergamon Press.

Hoffman, R. A. & Schmerling, E. R. 1981 *Dynamic Explorer* program: an overview. *Dynamic Explorer Space Sci. Instrum.* **5**, 345–348.

Killeen, T. L., Hays, P. B., Spencer, N. W. & Wharton, L. E. 1983 Neutral winds in the polar thermosphere as measured from *Dynamics Explorer. Adv. Space Res.* **2**, 133–136.

Killeen, T. L., Heelis, R. R., Hays, P. B., Spencer, N. W. & Hanson, W. B. 1985 Neutral motions in the polar thermosphere for northward interplanetary magnetic field. *Geophys. Res. Lett.* **12**, 159–162.

Killeen, T. L., Smith, R. W., Spencer, N. W., Meriwether, J. W., Rees, D., Hernandez, G., Hays, P. B., Cogger, L. L., Sipler, D. P., Biondi, M. A. & Tepley, C. A. 1986 Mean neutral circulation in the winter polar F-region. *J. geophys. Res.* **91**, 1633–1649.

Killeen, T. L., Craven, J. D., Frank, L. A., Ponthieu, J.-J., Spencer, N. W., Heelis, R. A., Brace, L. H., Roble, R. G., Hays, P. B. & Carignan, G. R. 1988 On the relationship between the dynamics of the polar thermosphere and the morphology of the aurora: global scale observations from *Dynamics Explorers* 1 and 2. *J. geophys. Res.* **93**, 2675–2692.

Krehbiel, J. P., Brace, L. H., Theis, R. F., Pinkus, W. H. & Kaplan, R. B. 1981 The *Dynamics Explorer* Langmuir probe instrument. *Space Sci. Instrum.* **5**, 493–502.

Mayr, H. G. & Volland, H. 1972 Theoretical model for the latitude dependence of the thermospheric annual and semi-annual variations. *J. geophys. Res.* **77**, 6774–6790.

Meriwether Jr, J. W. 1983 Observations of thermospheric dynamics from ground and space. *Radio Sci.* **18**, 1035–1052.

Meriwether Jr, J. W., Shih, P., Killeen, T. L., Wickwar, V. B. & Roble, R. G. 1984 Nighttime thermospheric winds over Sondre Stromfjord, Greenland. *Geophys. Res. Lett.* **11**, 931–934.

Meriwether, J. W., Biondi, M. A. & Anderson, D. N. 1985 Equatorial airglow depletions induced by thermospheric winds. *Geophys. Res. Lett.* **12**, 487–490.

Pereira, E., Kelley, M. C., Rees, D., Mikkelson, I. S., Jorgensen, T. S. & Fuller-Rowell, T. J. 1980 Observations of neutral wind profiles between 115 and 176 km altitude in the dayside auroral oval. *J. Geophys. Res.* **85**, 2935–2940.

Quegan, S., Bailey, G. J., Moffett, R. J., Heelis, R. A., Fuller-Rowell, T. J., Rees, D. & Spiro, R. W. 1982 Theoretical study of the distribution of ionization in the high-latitude ionosphere and the plasmasphere: first results on the mid-latitude trough and the light-ion trough. *J. atmos. terr. Phys.* **44**, 619–640.

Quegan, S., Bailey, G. J., Moffett, R. J. & Wilkinson, L. C. 1986 Universal Time effects on the plasma convection in the geomagnetic frame. *J. atmos. terr. Phys.* **48**, 25–40.

Rees, D. 1971 Ionospheric winds in the auroral zone. *J. Br. interplanet. Soc.* **24**, 233–346.

Rees, D. 1973 Neutral wind structure in the thermosphere during quiet and disturbed geomagnetic periods. In *Physics and Chemistry of Upper Atmospheres* (ed. B. M. McCormac), pp. 11–23. Dordrecht: Reidel.

Rees, D. & Fuller-Rowell, T. J. 1987*a* Comparison of theoretical models and observations of the thermosphere and ionosphere during extremely disturbed geomagnetic conditions during the last solar cycle. *Adv. Space Res.* **7**, 827–838.

Rees, D. & Fuller-Rowell, T. J. 1987*b* A theoretical thermosphere model for CIRA. *Adv. Space Res.* **7**, 10185–10197.

Rees, D., Fuller-Rowell, T. J. & Smith, R. W. 1980 Measurements of high-latitude thermospheric winds by rocket and ground-based techniques and their interpretation using a three-dimensional time-dependent dynamical model. *Planet. Space Sci.* **28**, 919–932.

Rees, D., McWhirter, I., Rounce, P. A. & Barlow, F. E. 1981 Miniature imaging photon detectors II: devices with transparent photocathodes. *J. Phys. Sci. Instrum.* **14**, 229–233.

Rees, D., Fuller-Rowell, T. J., Lyons, A., Killeen, T. L. & Hays, P. B. 1982 Stable and rugged etalon for the *Dynamics Explorer* Fabry–Perot Interferometer: I design and construction. *Appl. Optics* **21**, 3896–3902.

Rees, D., Fuller-Rowell, T. J., Gordon, R., Killeen, T. L., Hays, P. B., Wharton, L. E. & Spencer, N. W. 1983 A comparison of the wind observations from the *Dynamics Explorer* satellite with the predictions of a global-time dependent model. *Planet. Space Sci.* **31**, 1299–1314.

Rees, D., Lloyd, N., Charlton, P. J., Carlson, M., Murdin, J. & Haggstrom, I. 1984 Comparison of plasma flow and thermospheric circulation over northern Scandinavia using EISCAT and a Fabry-Perot interferometer. *J. atmos. terr. Phys.* **46**, 545–564.

Rees, D., Gordon, R., Fuller-Rowell, T. J., Smith, M. F., Carignan, G. R., Killeen, T. L., Hays, P. B. & Spencer, N. W. 1985 The composition, structure, temperature and dynamics of the upper thermosphere in the polar regions during October to December 1981. *Planet. Space Sci.* **33**, 617–666.

Rees, D., Fuller-Rowell, T. J., Gordon, R., Smith, M. F., Heppner, J. P., Maynard, N. C., Spencer, N. W., Wharton, L. E., Hays, P. B. & Killeen, T. L. 1986 A theoretical and empirical study of the response of the high-latitude thermosphere to the sense of the *Y*-component of the interplanetary magnetic field. *Planet. Space Sci.* **34**, 1–40.

Rees, D., Lloyd, N. D., Fuller-Rowell, T. J. & Steen, A. 1987 Observations of the variations of thermospheric winds in northern Scandinavia between 1980 and 1986: a study of geomagnetic activity effects during the last solar cycle. *Adv. Space Sci.* **7**, 39–47.

Rees, D., Fuller-Rowell, T. J., Quegan, S., Moffett, R. J. & Bailey, G. J. 1988 Simulations of the seasonal variations of the thermosphere and ionosphere using a coupled, three-dimensional, global model, including variations of the interplanetary magnetic field. *J. atmos. terr. Phys.* **50**, 903–930.

Rishbeth, H. 1972 Thermospheric winds and the F-region. *J. atmos. terr. Phys.* **34**, 1–47.

Roble, R. G., Dickinson, R. E. & Ridley, E. C. 1982 The global circulation and temperature structure of the thermosphere with high-latitude plasma convection. *J. geophys. Res.* **87**, 1599–1614.

Roble, R. G., Dickinson, R. E., Ridley, E. C., Emery, B. A., Hays, P. B., Killeen, T. L. & Spencer, N. W. 1983 The high-latitude circulation and temperature structure of the thermosphere near solstice. *Planet. Space Sci.* **31**, 1479.

Roble, R. G., Emery, B. A., Dickinson, R. E., Ridley, E. C., Killeen, T. L., Hays, P. B., Carignan, G. R. & Spencer, N. W. 1984 Thermospheric circulation, temperature, and compositional structure of the southern hemisphere polar cap during October–November 1981. *J. geophys. Res.* **89**, 9057–9068.

Smith, R. W. & Sweeney, P. J. 1978 Winds in the thermosphere of the northern winter polar cap. *Nature, Lond.* **284**, 437–438.

Spencer, N. W., Wharton, L. E., Nieman, H. B., Carignan, G. R. & Maurer, J. C. 1981 The *Dynamics Explorer* wind and temperature spectrometer. *Space Sci. Instrum.* **5**, 417–2428.

Tinsley, B. A., Sahai, Y., Biondi, M. A. & Meriwether, J. W. 1988 Equatorial particle precipitation during geomagnetic storms and relationship to equatorial thermospheric heating. *J. geophys. Res.* **93**, 270–276.

Watkins, B. J. 1978 A numerical computer investigation of the polar F-region. *Planet. Space Sci.* **26**, 559–569.

Wickwar, V. B., Meriwether Jr, J. W., Hays, P. B. & Nagy, A. F. 1984 The meridional thermospheric neutral wind measured by radar and optical techniques in the auroral region. *J. geophys. Res.* **89**, 10987–10998.

Wickwar, V. B., Johnson, R. M., Roble, R. G. & Luhmann, J. G. 1987 Lower-thermospheric winds at high latitude: Chatanika radar observations. *Annls Geophysicae* A **5** (6), 383–404.

Winser, K. J., Farmer, A. D., Rees, D. & Aruliah, A. 1989 Ion–neutral dynamics in the high-latitude ionosphere: first results from the INDI experiment. *J. atmos. terr. Phys.* (In the press.)

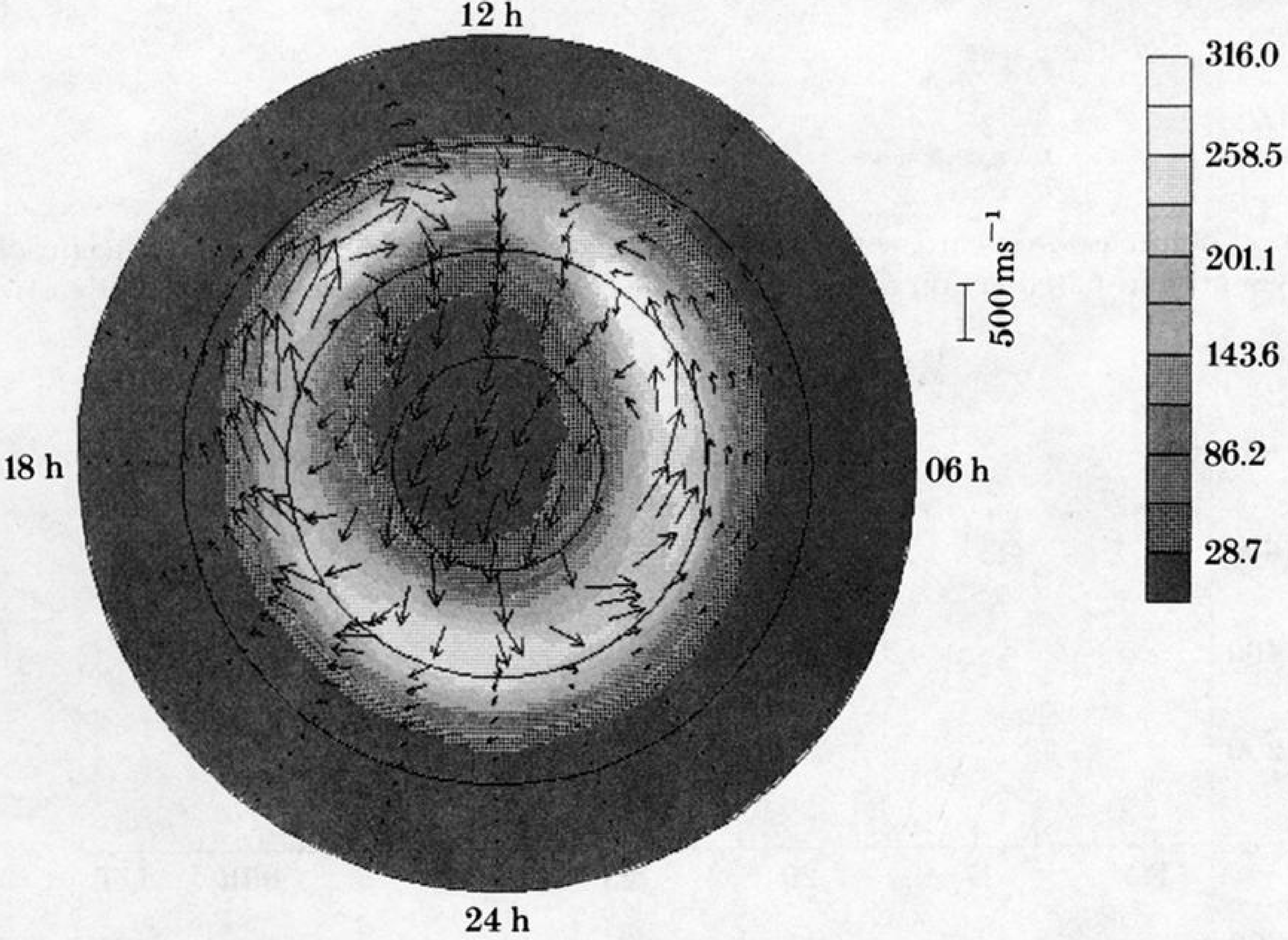

IGURE 2. Ionization rate (in units of 10^6 m^{-3}) and ion drift vectors associated with activity level 7 of figure 1, as they are mapped onto the geographic high latitudes (50–90°) by the IGRF magnetic field. Data is from the UCL–Sheffield model for equinox conditions and low solar activity ($F_{10.7} = 80$, 23 September).

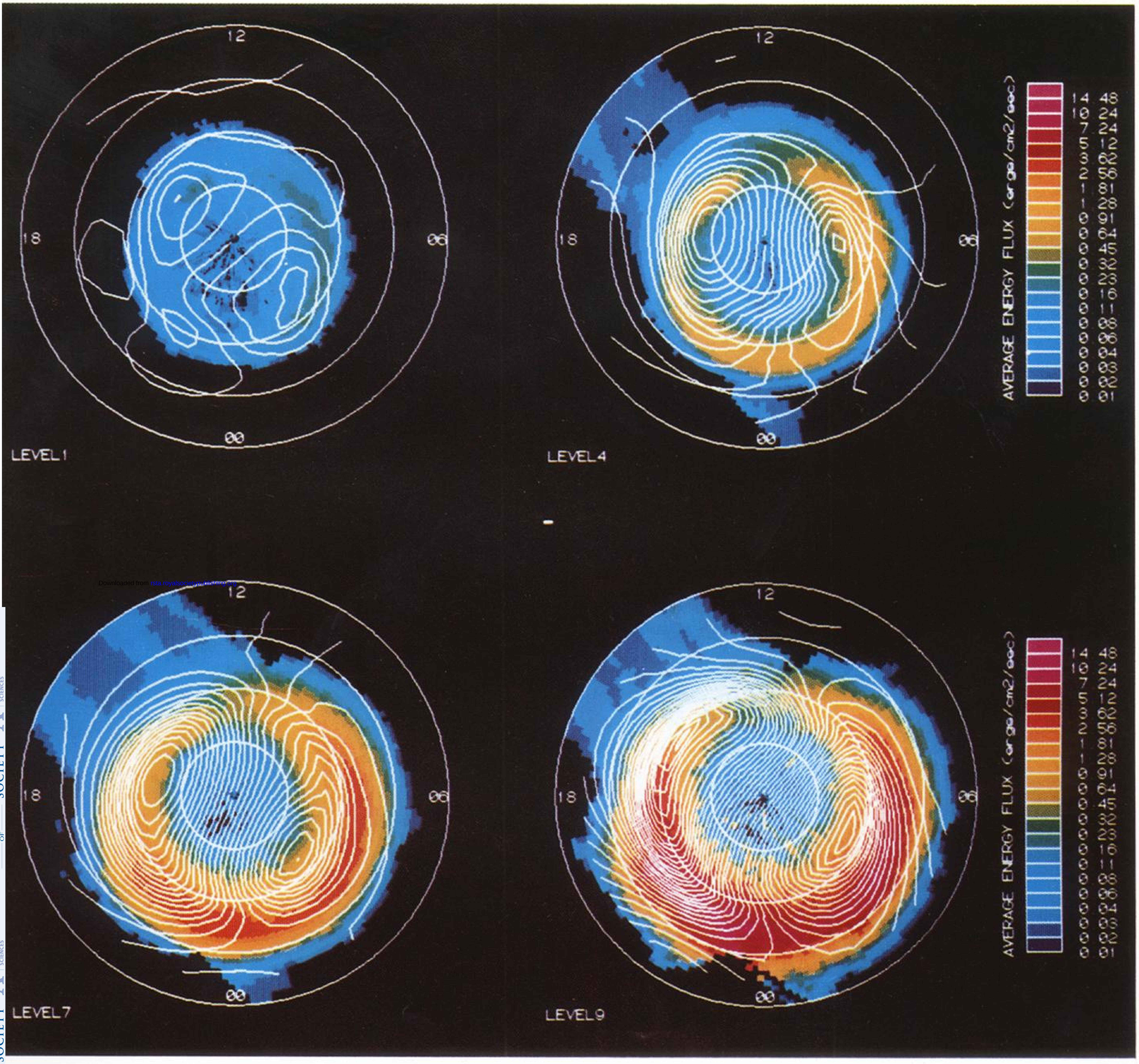

FIGURE 1. Statistical patterns of auroral particle energy influx (ergs per centimetre squared per second, 1 erg = 10^{-7} J) and equipotential convection contours for four increasing levels of geomagnetic activity.

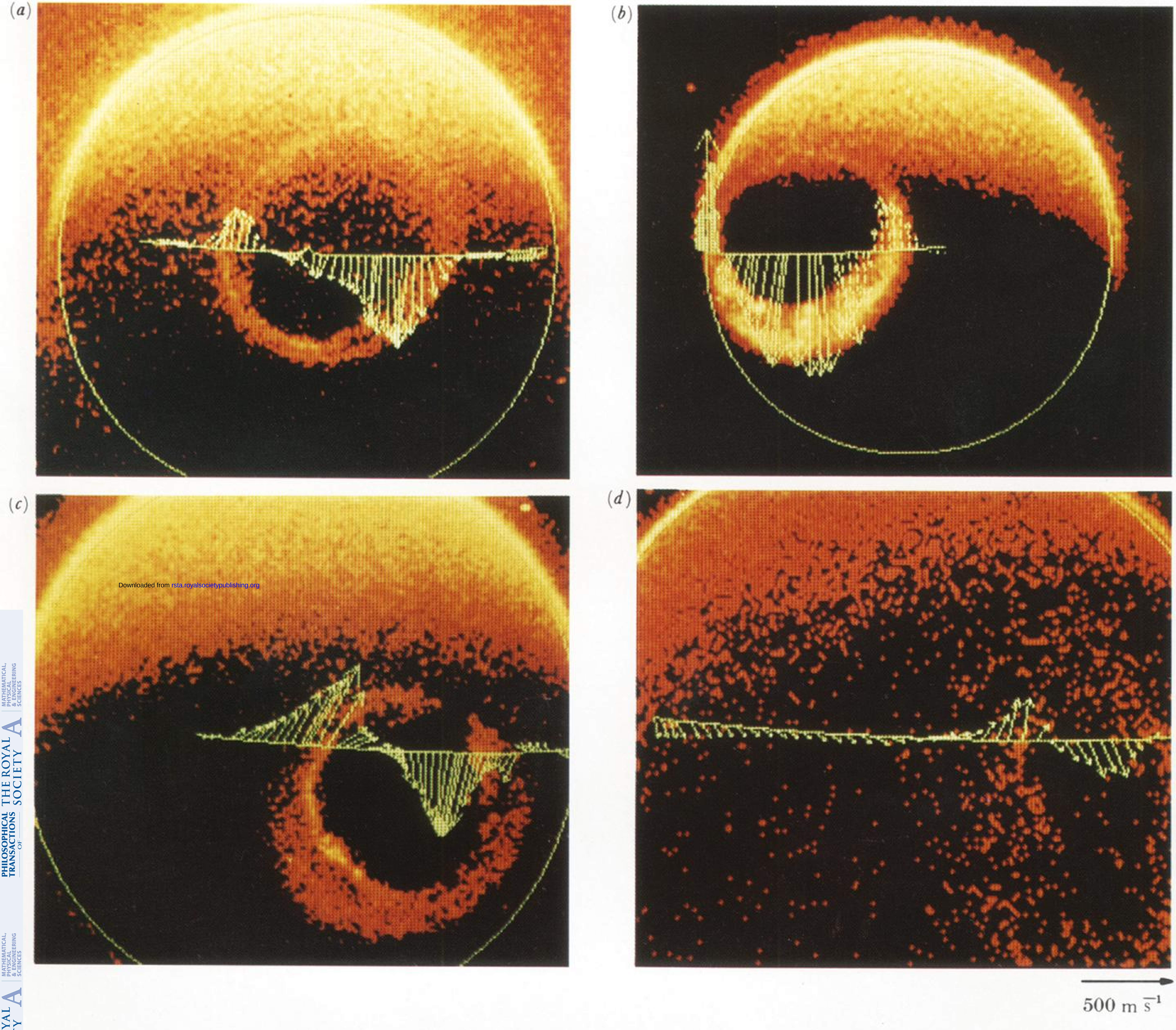

FIGURE 6. The *DE*2 and *DE*1 spacecraft simultaneously observed the northern auroral oval on a number of occasions during the winter of 1981–82 (Killeen *et al.* 1988). The observations were made on (*a*) 6 December 1981 at 15h05 U.T., orbit 1853; (*b*) 12 December 1981 at 12h44 U.T., orbit 1941; (*c*) 6 December 1981 at 08h38 U.T., orbit 1849; (*d*) 15 December 1981 at 05h05 U.T., orbit 1981. *DE*2 provided the wind vectors, while the large-scale auroral images were obtained from the *DE*1 spin-scan imager.

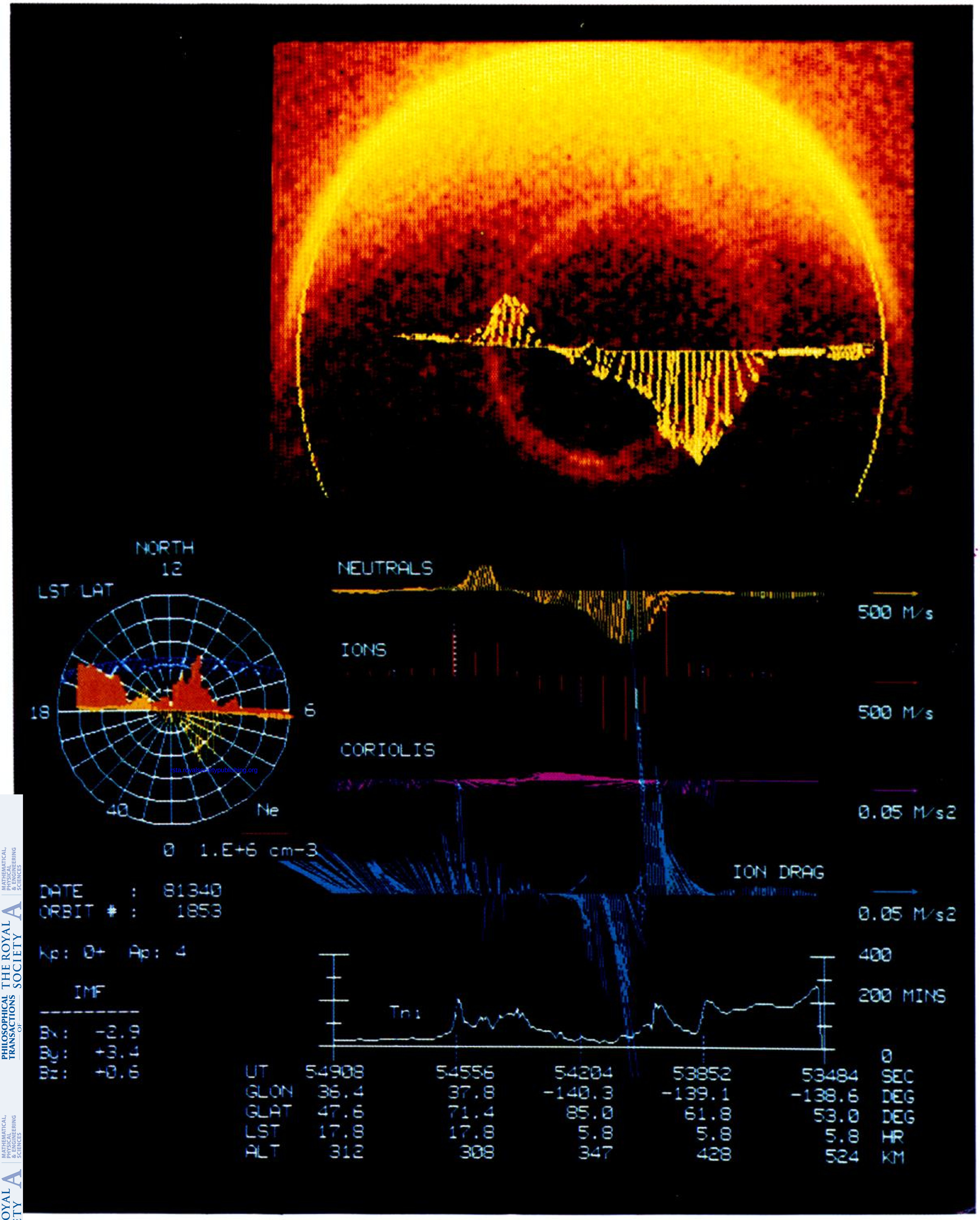

FIGURE 7. A detailed study of the situation shown in figure 6*a* (Killeen *et al.* 1988); day 340, 1981, orbit 1853. Properties of the thermal plasma (ion density and ion drift) within the polar region are shown, along with a determination of the ion–neutral collision time constant, $T_{\rm ni}$, and various important forces coupling the high-latitude ionosphere and thermosphere. $K_{\rm p}$ is 0^{+}; the IMF is $\boldsymbol{B} = (-2.9, +3.4, +0.6)$.

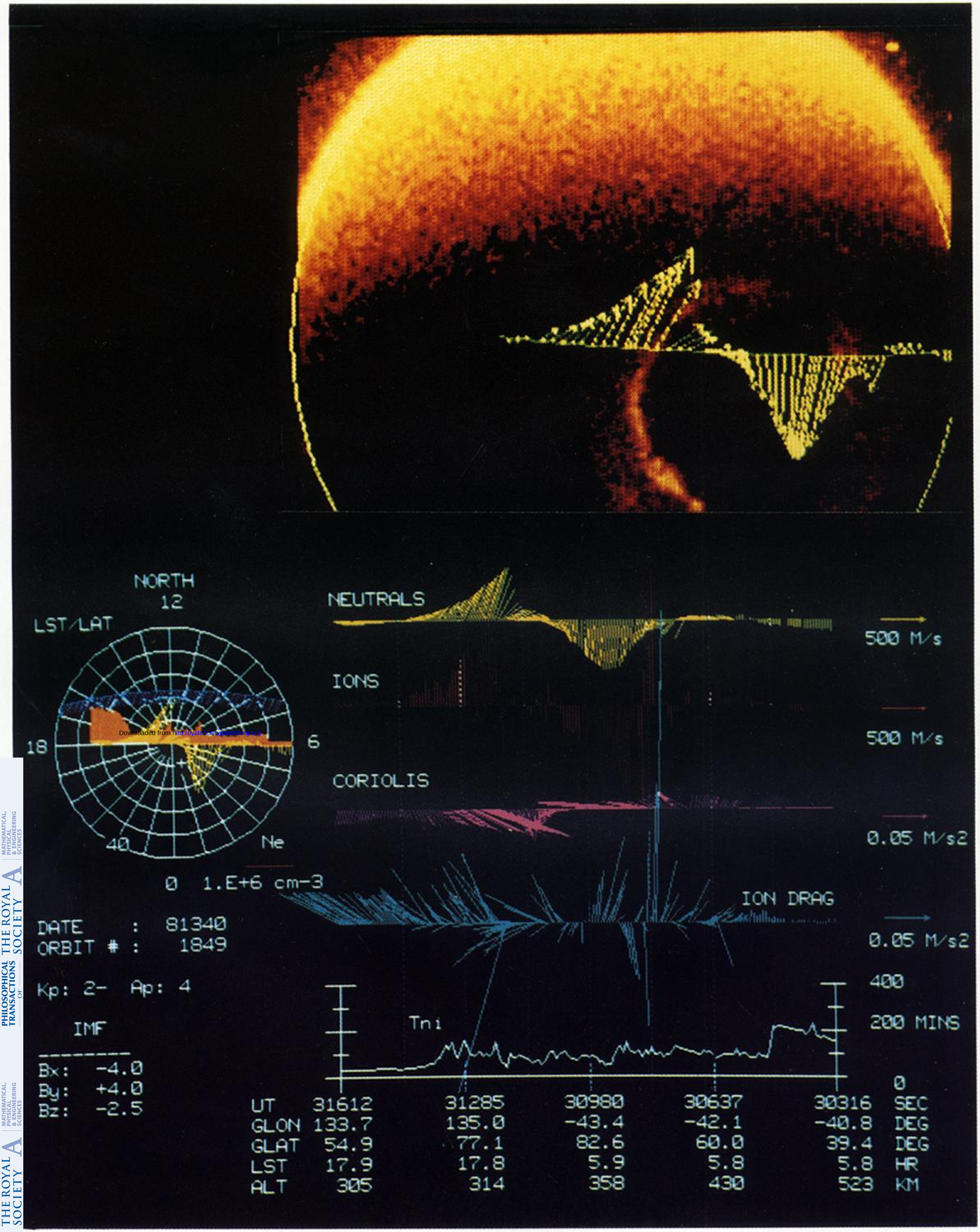

FIGURE 8. Polar dial plot of EISCAT data for 3–4 February 1984 on azimuth 1 (332°), in the same format as figure 3.

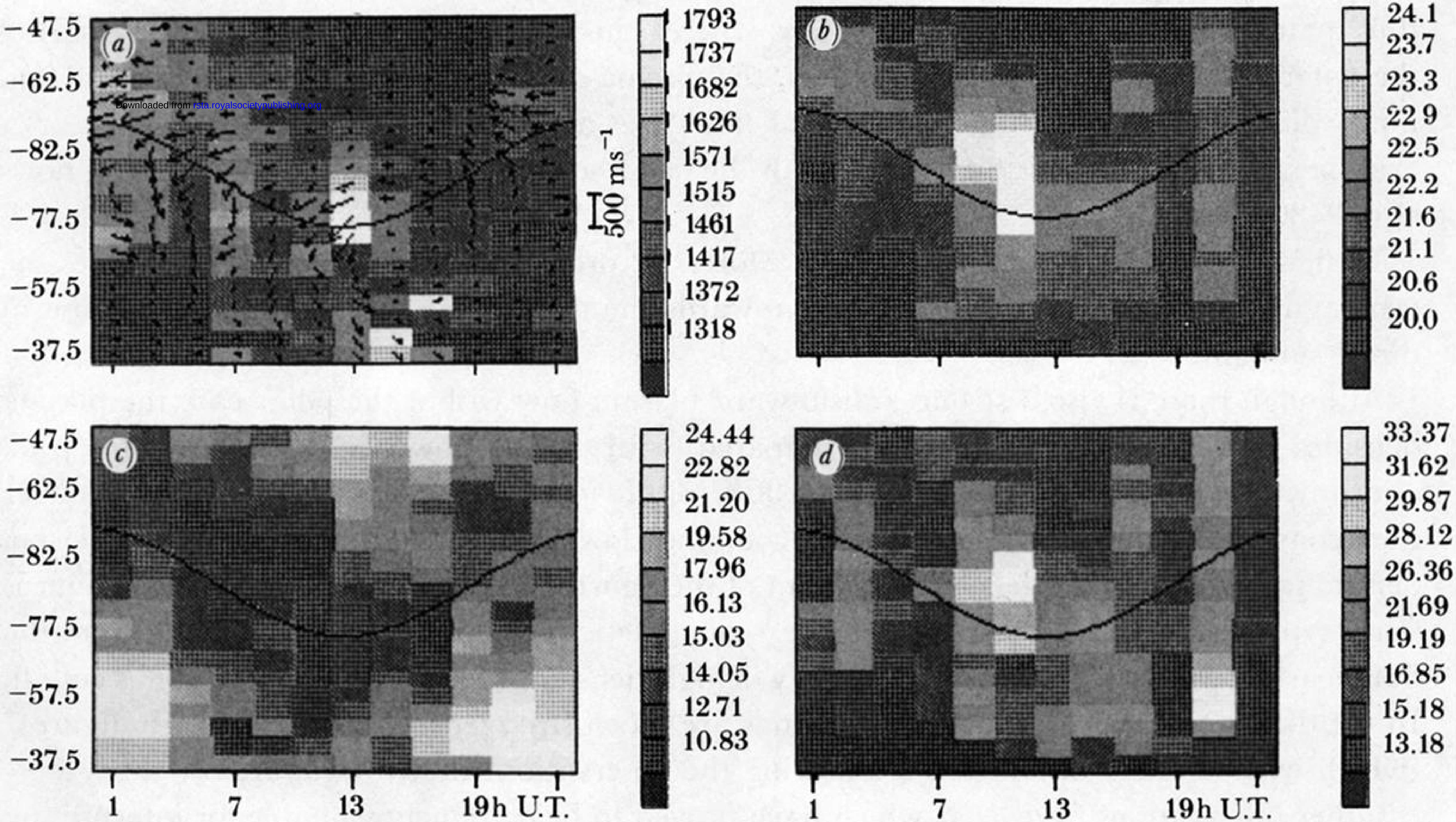

FIGURE 9. Statistical distributions of neutral composition, wind and temperature for the south polar region during October 1981 as observed by *DE2* in the 22.8–08.6h LT orbit plane. (*a*) Temperature plot (in kelvins); (*b*) molecular mass (in unified atomic mass units); (*c*) O_2 density and (*d*) N_2+O_2 density plots (in units of 10^{-12} kg m^{-3}).

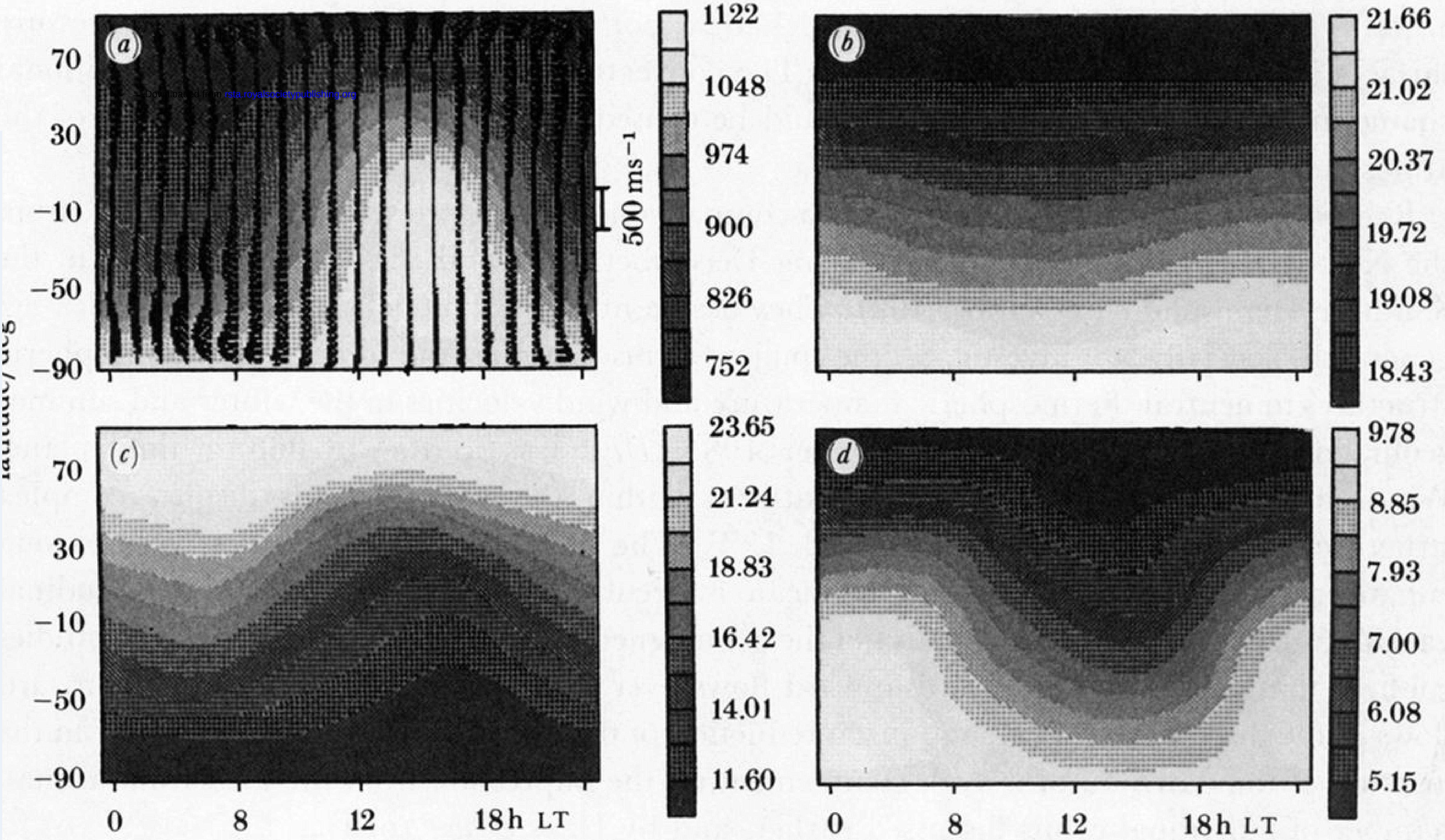

FIGURE 10. Simulation (three-dimensional coupled model) of neutral composition, wind and temperature in December, for pressure level 12 (*ca.* 300 km), at 18h U.T. and high solar activity ($F_{10.7} = 185$) and low geomagnetic activity. (*a*) Temperature plot (in kelvins); (*b*) molecular mass (in unified atomic mass units); (*c*) O_2 density and (*d*) $N_2 + O_2$ density plots (in units of 10^{-13} kg m^{-3}).

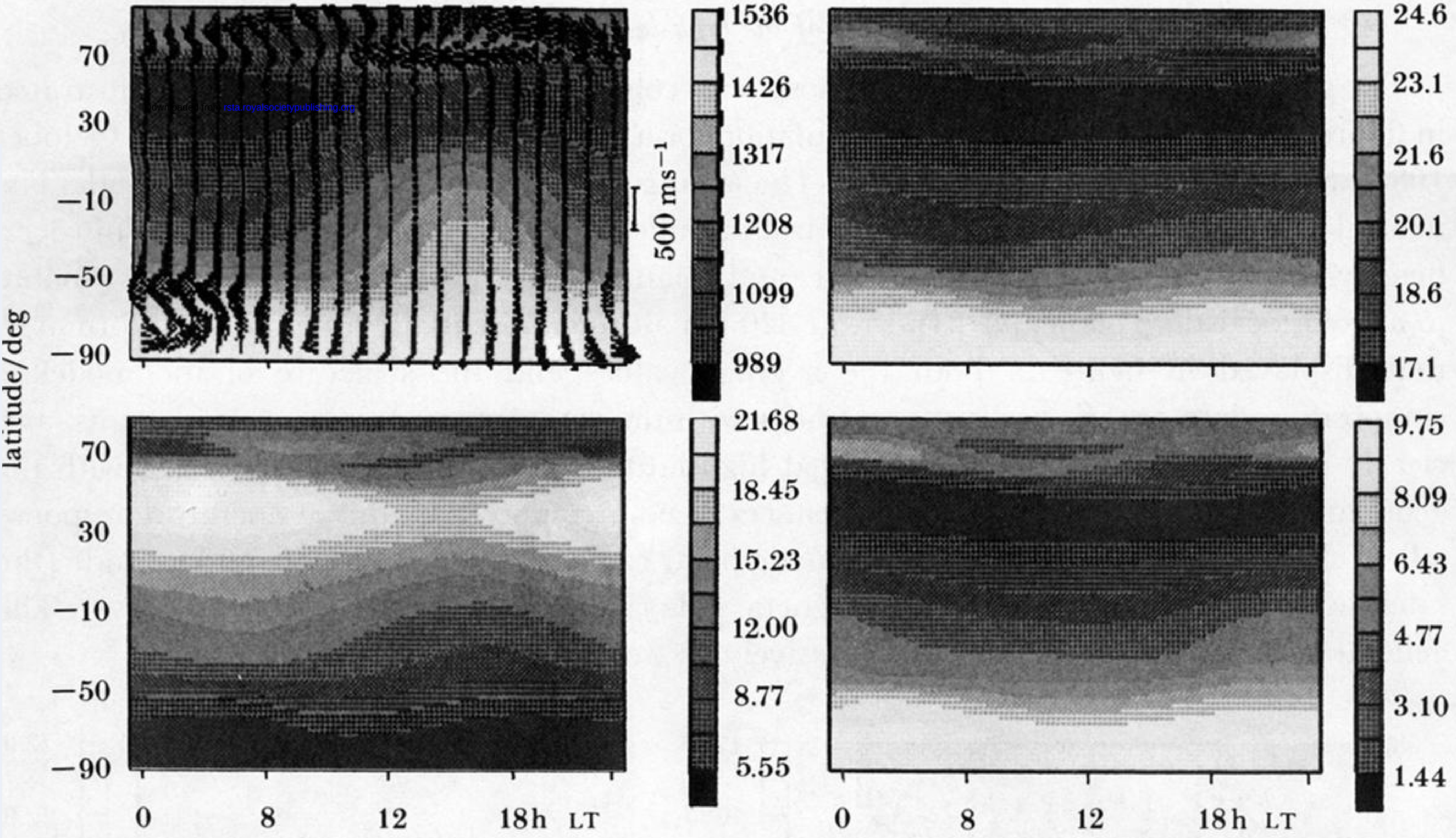

FIGURE 11. Model simulation of neutral composition, winds and temperature in December, for pressure level 12 (*ca.* 300 km), at 18h U.T. and high solar activity and moderate geomagnetic activity (K_p of 3^+). (*a*) Temperature plot (in kelvins); (*b*) molecular mass (in unified atomic mass units); (*c*) O_2 density and (*d*) N_2+O_2 density plots (in units of 10^{-12} kg m^{-3}).

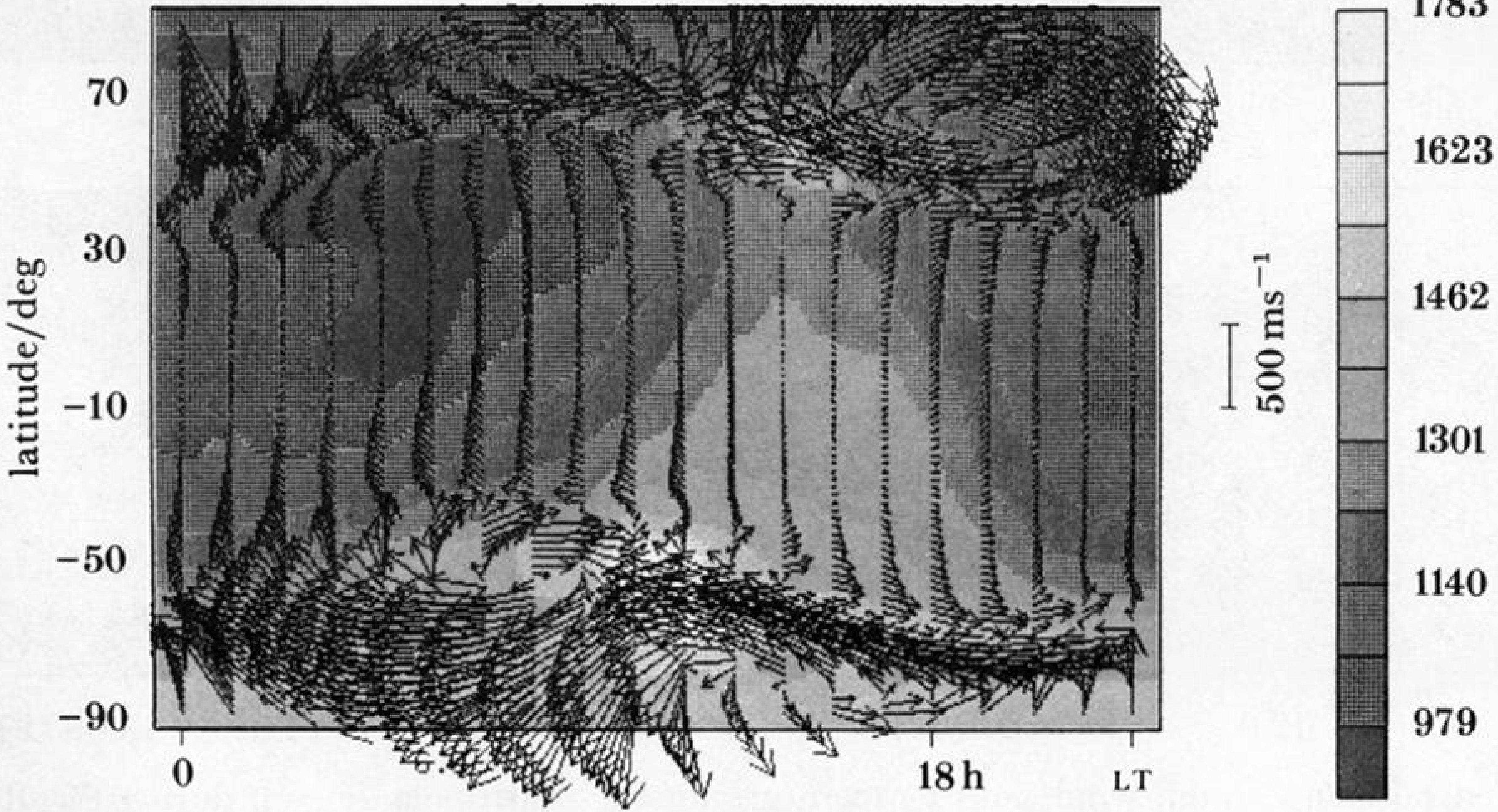

GURE 12. Model simulation of neutral composition, winds and temperature (in kelvins) in December, for pressure level 12 (*ca.* 300 km), at 0h U.T. and high solar activity ($F_{10.7} = 185$) after a period of very high geomagnetic activity.

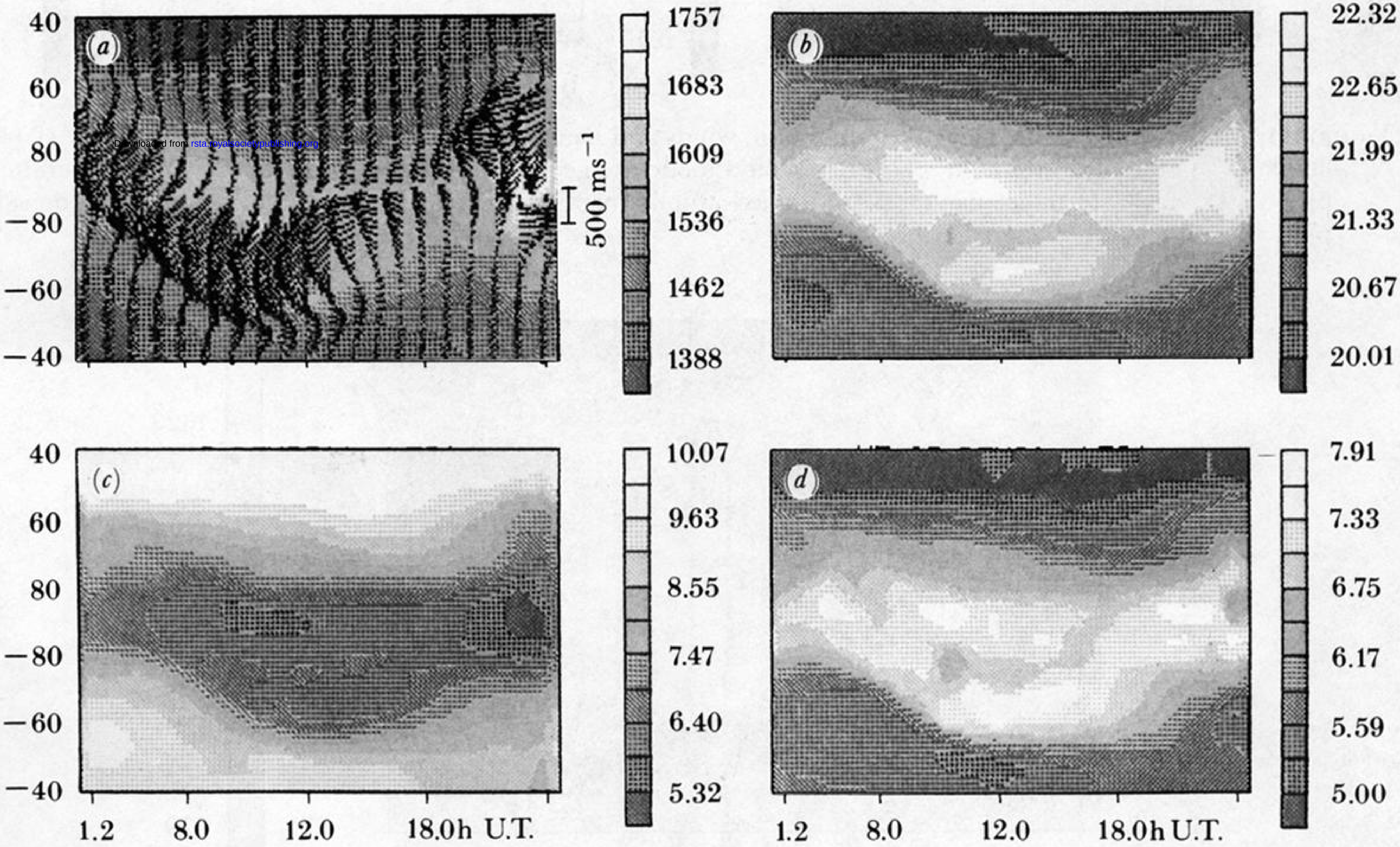

FIGURE 13. Neutral composition, winds and temperature for the south polar region during October 1981 in the 09–21h LT plane, as simulated by the thermospheric model (presented in the same format as figure 9). (*a*) Temperature plot (in kelvins); (*b*) molecular mass (in unified atomic mass units); (*c*) O_2 density and (*d*) N_2+O_2 density plots (in units of 10^{-13} kg m^{-3}).

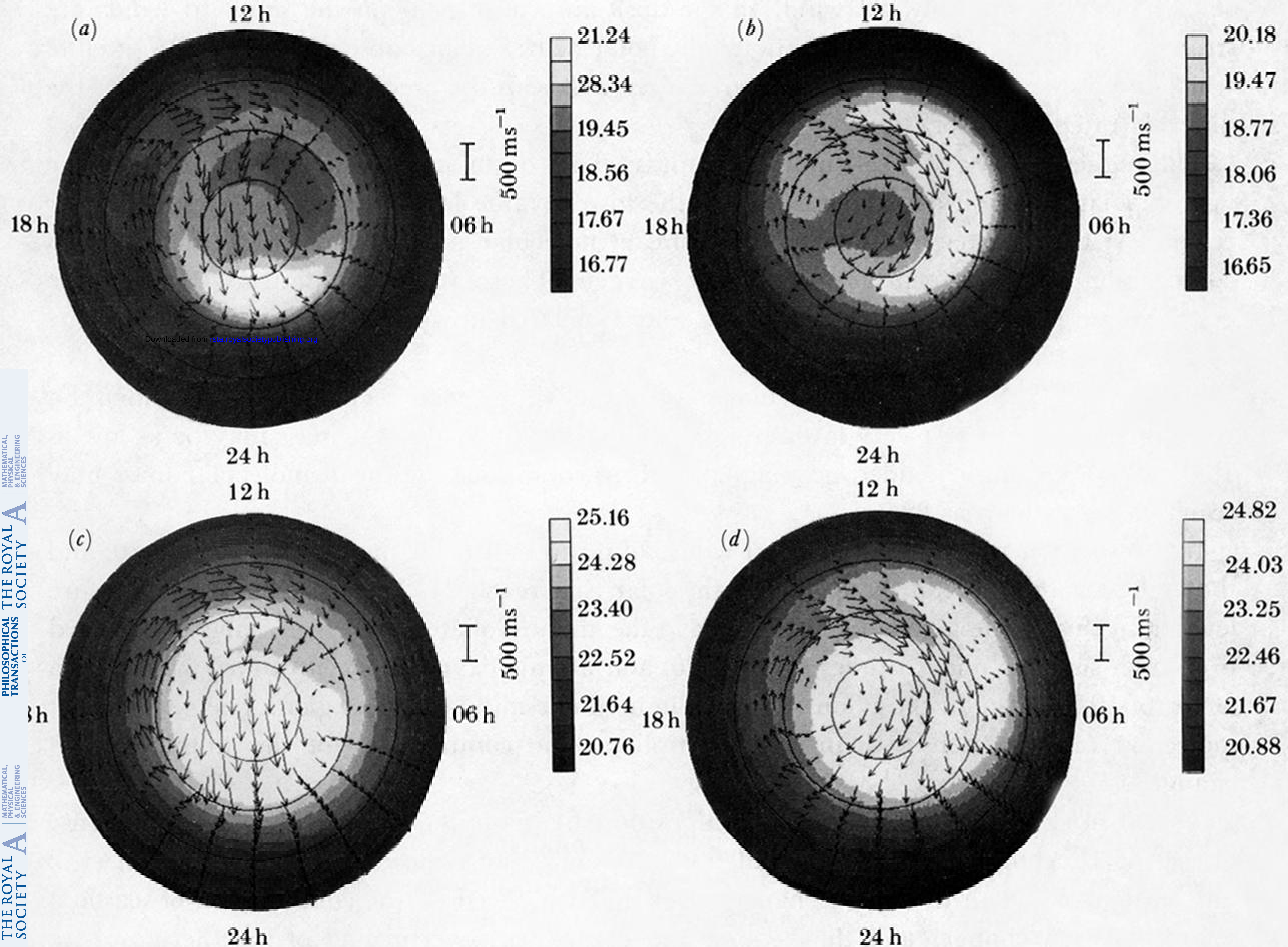

FIGURE 14. A montage of four plots, 50–90° latitude, of mean molecular mass (in unified atomic units) and neutral wind from the coupled model at pressure level 12, high solar activity ($F_{10.7} = 185$) and moderate geomagnetic activity (K_p of 3^+). (*a*) Winter B_y negative; (*b*) winter B_y positive; (*c*) summer B_y negative; (*d*) summer B_y positive. All at 18h U.T.

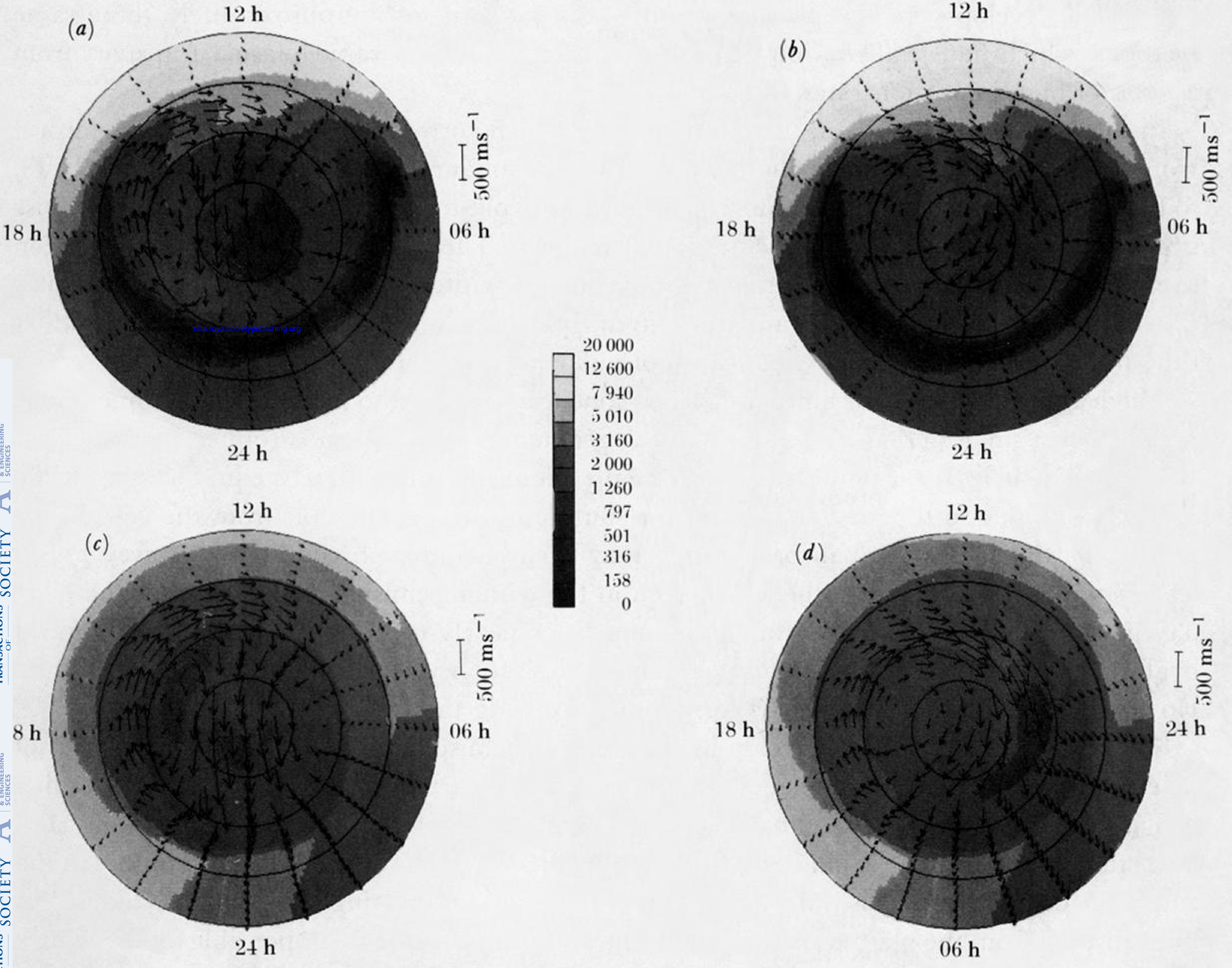

FIGURE 15. A montage of four plots, 50–90° latitude, of ion density (in units of 10^8 m^{-3}) and neutral wind from the coupled model at pressure level 12, high solar activity ($F_{10.7} = 185$) and moderate geomagnetic activity (K_p of 3^+). (*a*) Winter B_y negative; (*b*) winter B_y positive; (*c*) summer B_y negative; (*d*) summer B_y positive.

PHILOSOPHICAL TRANSACTIONS OF THE ROYAL SOCIETY A MATHEMATICAL, PHYSICAL & ENGINEERING SCIENCES

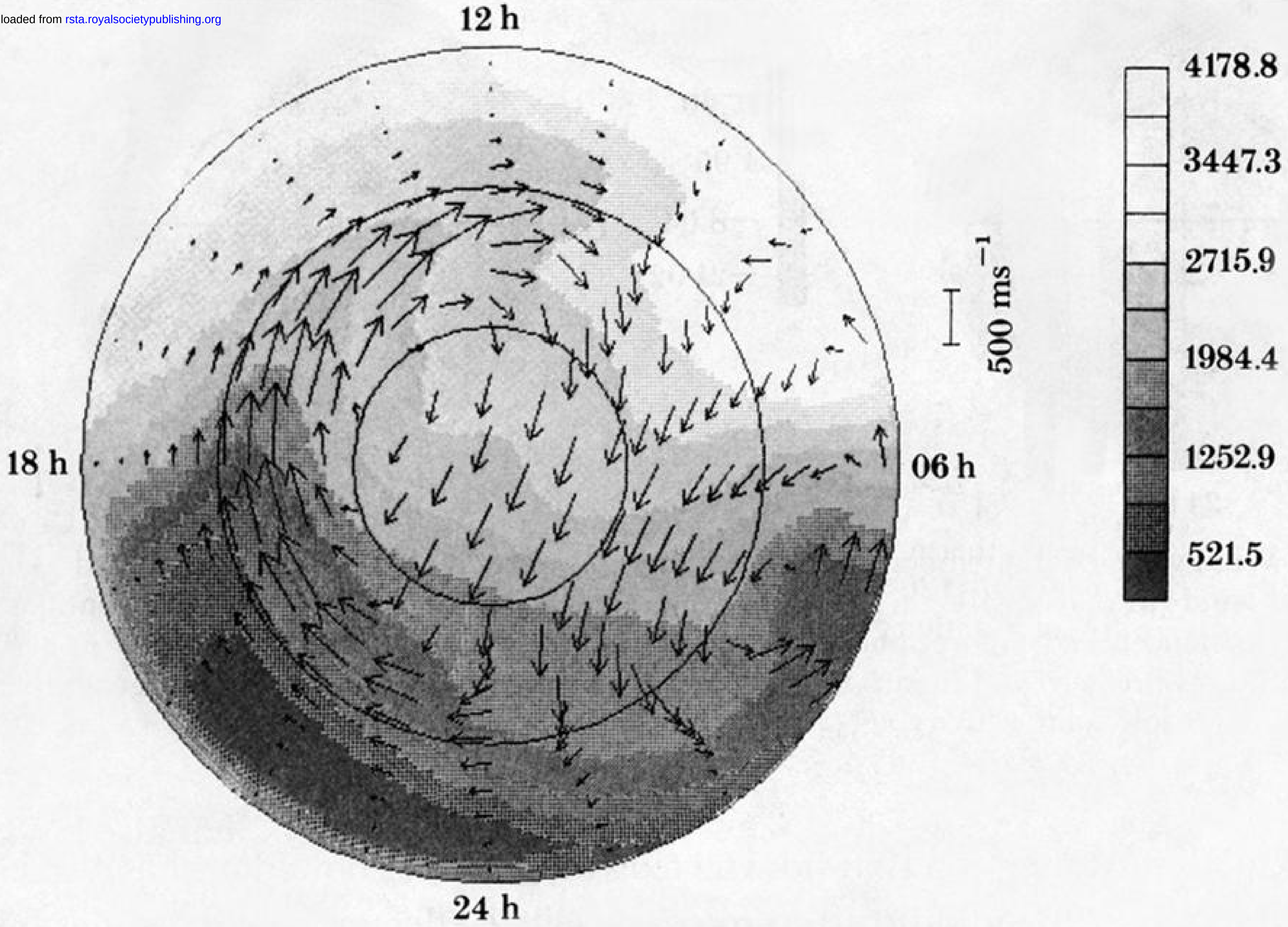

IGURE 16. Ion density (in units of 10^8 m^{-3}) and ion drifts in the northern polar region, 60–90° latitude, pressure level 12h U.T., close to the F-region peak, at low solar activity ($F_{10.7} = 80$) and moderate geomagnetic activity (K_p of 3^+).

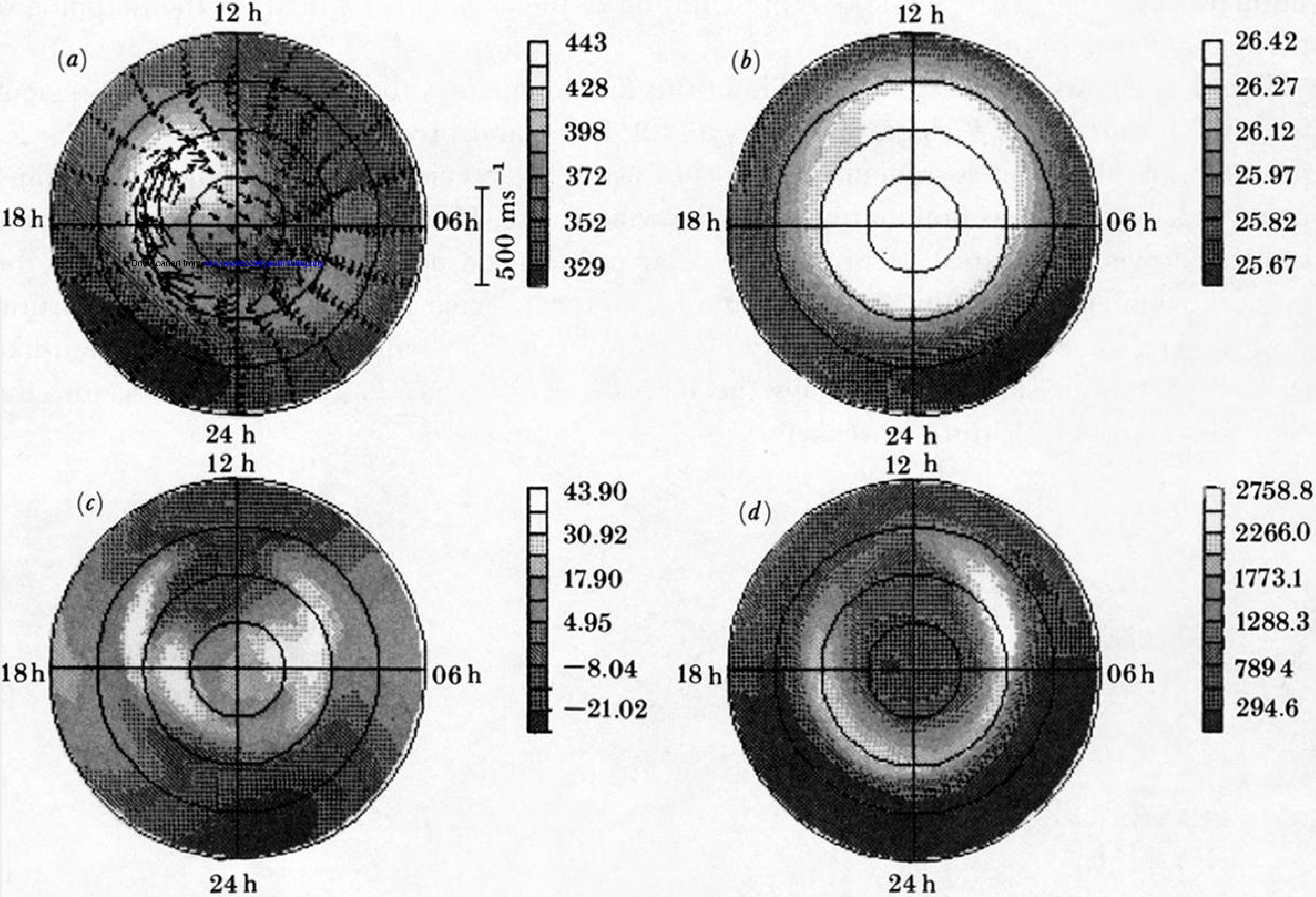

FIGURE 17. (*a*) Wind velocity and temperature (in kelvins); (*b*) mean molecular mass (in unified atomic mass units); (*c*) vertical wind (in units of 10^{-2} m s^{-1}); (*d*) plasma density (in units of 10^{8} m^{-3}) distributions taken from the UCL coupled ionosphere–thermosphere GCM simulation for equinox conditions for IMF B_y zero. The data are presented at pressure level 7 (120 km) for the northern polar region (poleward of 50° geographic latitude) and at 18h U.T., for low solar activity ($F_{10.7} = 80$) and moderate geomagnetic activity (K_p of 3^+).

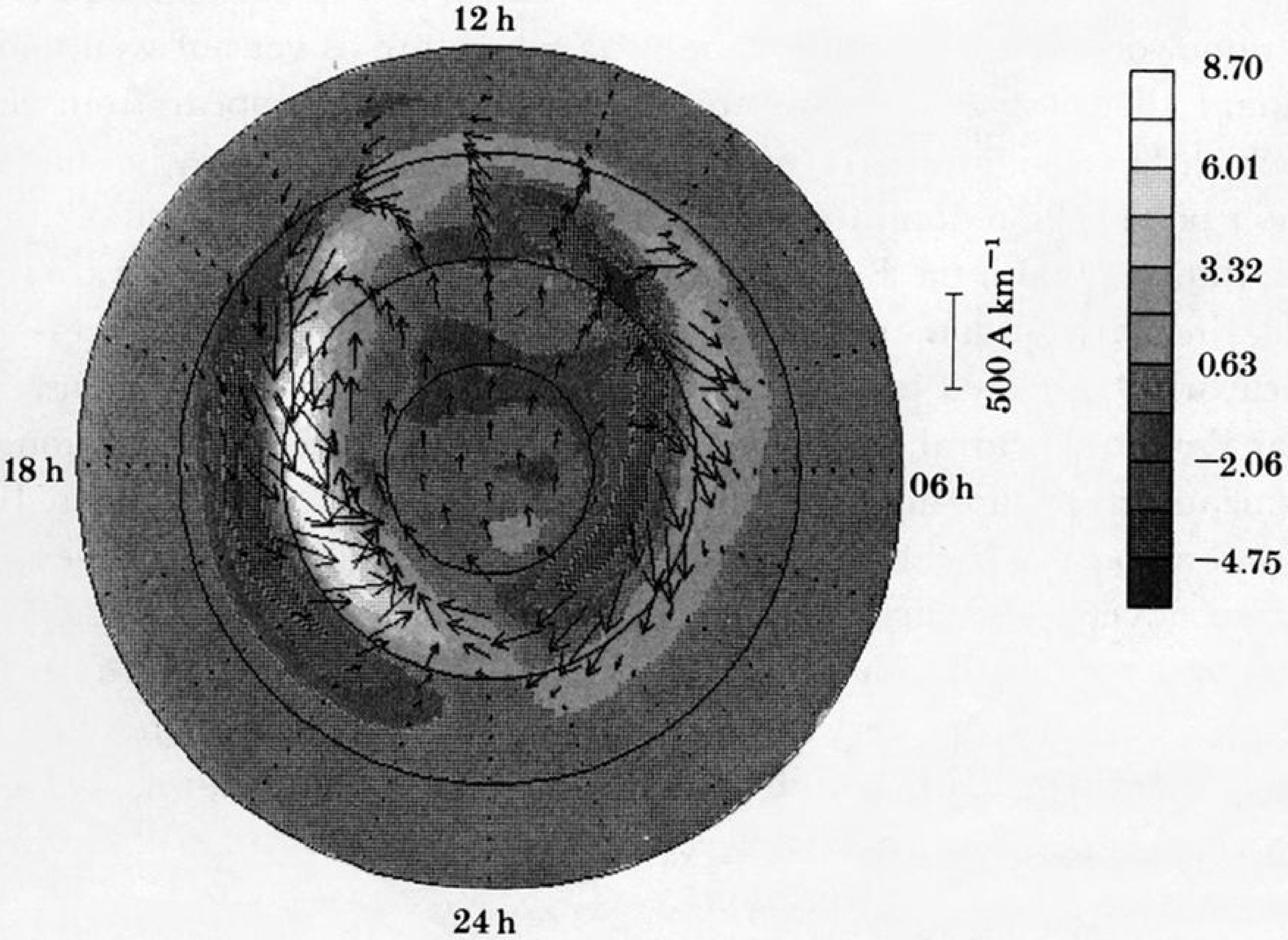

IGURE 18. The field-aligned current density (in units of 10^{-1} μA m^{-2}) in the high-latitude thermosphere, and the height-integrated current vectors, for the same conditions as figure 17.